Pergamon

J. Mech. Phys. Solids, Vol. 46, No. 6, pp. 1089–1124, 1998

Printed in Great Britain
0022–5096/98 $19.00+0.00

PII: S0022–5096(97)00060–4

ONSET OF FAILURE IN ALUMINUM HONEYCOMBS UNDER GENERAL IN-PLANE LOADING

N. TRIANTAFYLLIDIS* and M. W. SCHRAAD†

Department of Aerospace Engineering, The University of Michigan, Ann Arbor, Michigan 48109-2140, U.S.A.

(*Received* 29 *January* 1997; *in revised form* 30 *June* 1997)

ABSTRACT

Of interest here is the theoretical prediction of the onset of failure in aluminum honeycombs under arbitrary macroscopic loading conditions. A failure surface is defined in macroscopic stress space by the onset of the first buckling-type instability encountered along proportional load paths, where each load path is defined by a fixed macroscopic load orientation and a fixed ratio of principal macroscopic stresses. The influence of specimen size (i.e., geometric scale effects), and the influence of geometric microstructural imperfections on these failure surfaces, are investigated through a combination of analytical (i.e., Bloch wave) and numerical (i.e., finite element) techniques.

All of the analyses presented here are carried out for commercially available honeycombs, and the results show an extreme sensitivity of the onset of failure in these materials to the macroscopic load orientation and the principal macroscopic stress ratio. In addition, the failure surface for a perfectly periodic honeycomb of infinite extent, is found to be an upper bound for the failure surfaces of the corresponding finite honeycomb specimens with microstructural imperfections. Moreover, the construction of the failure surfaces for the imperfect specimens requires the numerical solution for large, multicell models, while the failure surface for the finite, perfectly periodic model is obtained with less computational effort, since calculations involving only the unit cell are required. The methodology proposed in this investigation, therefore, provides a useful predictive tool for the design of these materials.

Keywords: A. buckling, A. microstructures, B. elastic–plastic material, B. finite deflections, B. foam material.

1. INTRODUCTION AND MOTIVATION

Low density cellular solids, both natural and synthetic, are widely used in engineering applications, due mainly to their high stiffness-to-weight ratios. During the last two decades in particular, the manufacture and use of synthetic cellular materials have undergone enormous growth. These materials, which form an interconnected network of solid struts and plates (the edges and faces of the cells, respectively), can be broadly categorized into two groups. The first group, termed "honeycombs", consists of cellular materials with essentially two-dimensional microstructures, while the second group, termed "foams", includes those materials with fully three-dimensional micro-

* Author to whom correspondence should be addressed.

† Currently: Group T-3, Mail Stop B216, Theoretical Division, Los Alamos National Laboratory, Los Alamos, New Mexico 87545.

structures. Until recently, synthetic cellular solids were manufactured primarily from polymers. Due to advances in materials science, however, cellular solids are now manufactured from ceramics, metals, and many other materials as well. In addition to their high stiffness-to-weight ratios, cellular materials, when subjected to compression, have excellent shock mitigation and energy absorption characteristics. As a result of these mechanical advantages, cellular materials are increasingly used in aerospace applications which require lightweight and high performance, and are virtually indispensable in all types of packaging applications for product transportation purposes.

In spite of the long established and widespread use of cellular solids in engineering and structural applications, the study of their mechanical properties, and in particular the behavior of these materials under compression, is still in its relative infancy. Among the first important investigations in these areas are the works of Gent and Thomas (1963), Shaw and Sata (1966), and Patel and Finnie (1970). The book edited by Hilyard (1982) contains a series of articles which summarize the state of the art (at that period of time) for polymeric foams. Credit for refocusing the attention of the research community to the mechanics of cellular materials, must be given to Gibson and Ashby (1988) for their excellent monograph which presents a comprehensive study of the structure, the properties, and the mechanical behavior of a wide range of honeycombs and foams, both natural and synthetic. The mechanics of honeycombs, which are of particular interest to the present work, have been studied more recently, both analytically and experimentally, and have been explored in greater detail by Ashby, Gibson, and their coworkers (e.g., Ashby, 1983; Gibson and Ashby, 1982; Gibson *et al.*, 1982, 1989; Triantaffilou *et al.*, 1989), by Klintworth and Stronge (1988, 1989), and by others.

The aforementioned works constitute an excellent starting point for the subject at hand. Due to their broad scope, however, these investigations do not always address, in depth, the various mechanisms involved at the different stages of deformation in cellular solids. In particular, the crucial role played by instabilities, which are due to strong material and geometric nonlinearities, and which lead to microbuckling, followed by a localized failure mode, is not given appropriate attention. These issues have recently been addressed by Papka and Kyriakides (1994), who have conducted a series of careful experimental and theoretical investigations involving aluminum honeycombs under in-plane, uniaxial compression. Their work has shown that a consideration of plasticity, and geometric nonlinearities, can result in a significant reduction in the initial buckling load of the honeycomb material, as compared to the simpler, Euler-type, elastic buckling loads obtained in the previously mentioned references. Moreover, their work has also shown that the localized failure mode is due to the subcritical (i.e., occurring under a lower than critical load) nature of the postbuckling behavior of the unit cell. Full scale numerical calculations, involving finite sized honeycomb specimens, complete their experimental studies, by modeling the deformation of the honeycomb specimens from rest, through initial bifurcation and subsequent localization of deformation in a row of cells, all the way to complete collapse of the entire specimen. Their work, in addition to all of the previously mentioned research, however, pertains to uniaxial or biaxial loading aligned with the initial axes of orthotropy of the honeycomb material. Important issues concerning the dependence of the mechanical behavior of these materials on the macroscopic

load orientation and the specimen size have not been systematically addressed, to the best of the authors' knowledge.

On the theoretical side, the motivation for the present work stems from some closely related, earlier research, conducted by the first author, on the stability of finitely strained, rate-independent, periodic composite materials. The periodic nature of their microstructure allows exact calculations for the onset of instability in these solids, under arbitrary macroscopic loading conditions. Given that the onset of a bifurcation-type instability is the precursor to the ultimate failure mode in these materials, it seems logical to investigate the critical macroscopic stress state, and also to determine the nature of the corresponding critical bifurcation mode. The critical mode for an infinite, perfectly periodic medium is characterized by a dimensionless wave number ω_c, which is defined as the ratio of the unit cell size to the wavelength of the bifurcation mode shape. The value of this wave number provides an indication as to whether or not a localized failure mode is possible. Moreover, a theoretical failure surface can be constructed in macroscopic stress or macroscopic strain space, based on calculations involving only the unit cell, for any rate-independent, perfectly periodic composite of infinite extent. The usefulness of this failure surface for applications lies in the fact that it provides an upper bound for the onset of failure in the corresponding actual composite materials, which necessarily contain imperfections in the periodicity of their underlying microstructures (see Schraad and Triantafyllidis, 1997).

More specifically, for the simplest possible microgeometry (i.e., for the case of axially deformed, layered composites under plane strain conditions), the corresponding analytical determination of the critical dimensionless wave number ω_c was given by Triantafyllidis and Maker (1985). Subsequent work by Geymonat *et al.* (1993), has illustrated the completeness of the Bloch wave representation for capturing the initial instability in finitely strained, rate-independent, perfectly periodic composites in three dimensions, and has proven that, in the case for which $\omega_c \to 0$, the first instability can also be determined from the macroscopic properties of the infinite medium, as the first loss of ellipticity in the homogenized moduli of the material. Lastly, the concepts of the micro- and macro-failure surfaces in macroscopic stress or macroscopic strain space for finitely strained, periodic media, were introduced by Triantafyllidis and Schnaidt (1993), for the case of biaxially loaded frame models.

All of the aforementioned research concerns perfectly periodic media of infinite extent. The influence of specimen size, also termed the "geometric scale effect", and the influence of microstructural imperfections on the onset of failure in these materials have not been addressed systematically, since the required calculations are orders of magnitude more complicated. These topics were the subject of a recent investigation by the present authors (see Schraad and Triantafyllidis, 1997), in which all of the calculations were, for reasons of computational efficiency, based on simple, two-dimensional lattice models. The use of aluminum honeycombs in engineering and structural applications makes these materials an excellent subject for the extension of the previously described general ideas, concerning the stability of periodic and nearly periodic media, to an actual microstructured material.

The present investigation pertains to the stability, and the associated geometric scale effects and imperfection sensitivity of aluminum honeycombs, which exhibit rate-independent, elasto-plastic stress–strain behavior, and which are subjected to

arbitrary, in-plane, macroscopic stress states. The outline of the work is as follows. Presented in Section 2 is the general formulation of the principal solution and the initial bifurcation instability for a hexagonal cell honeycomb material of infinite extent. In Section 3, following a description of the numerical algorithm used in the present calculations, the principal solutions for the infinite honeycomb models, as well as the corresponding onset of plasticity and maximum load surfaces, determined under general, in-plane loading conditions, are discussed. Next, the initial bifurcation surfaces for the infinite honeycomb models are examined, followed by an investigation of the geometric scale effects on these failure surfaces. Finally, the influence of imperfections in the material microstructure on the initial bifurcation surfaces of the honeycomb models are explored. The presentation is then concluded in Section 4 with a detailed discussion of the results, and suggestions for future research.

2. PROBLEM FORMULATION

Presented in this section is the general formulation of the principal solution and the onset of instability for hexagonal cell, honeycomb specimens. Contained in the first part of this section is a discussion concerning the geometry of the models, the material properties, and the imposed loading conditions. In the second part, the initial bifurcation problem for a perfectly periodic honeycomb model of infinite extent is formulated, under the conditions of general in-plane loading.

2.1. *Model description and loading conditions*

A typical planar section (i.e., a section perpendicular to the cell walls) of a perfectly periodic honeycomb material, which consists of a regular hexagonal lattice, is shown in Fig. 1(a). The cell walls are very thin (thickness-to-length ratios are typically of the order of 0.01), and for the loading presently considered, deform essentially through bending. Consequently, each cell wall of the honeycomb material is idealized as a nonlinear beam, capable of undergoing arbitrarily large displacements and rotations. The corresponding beam theory is a generalization of the elastica beam theory due to Euler, which allows for axial deformations as well. This theory has already been proposed elsewhere (see, for example, Love, 1944; Antman, 1968), however, for reasons of completeness, a short presentation of the theory is included here.

Consider an initially straight beam of length l and thickness t (the width of the beam is taken to be $h = 1$), as shown in Fig. 1(b). Due to the action of the forces and moments at the ends of the beam (i.e., at points A and B in Fig. 1(b)), a point on the middle line of the beam (shown as a dotted line in Fig. 1(b)), initially at distance s from end A, displaces by $v(s)$ and $w(s)$ along the tangential and normal directions to the initial configuration, respectively. By adopting the classic Bernoulli–Navier–Euler hypotheses, that cross-sections perpendicular to the initial middle line remain perpendicular to the deformed middle line, and undergo negligible extension, the axial strain $\varepsilon(s, z)$ at a material point with initial coordinates (s, z) is found to be

$$\varepsilon = e + zk. \tag{1}$$

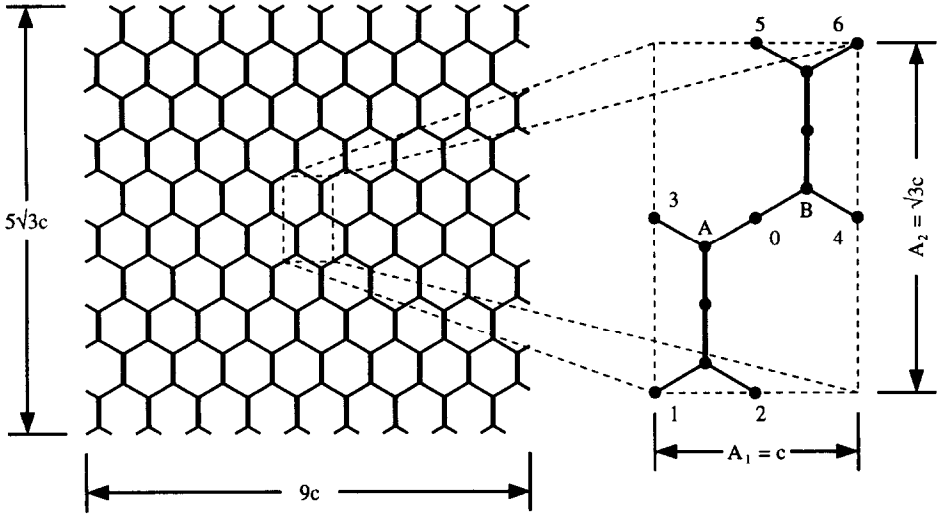

(a)

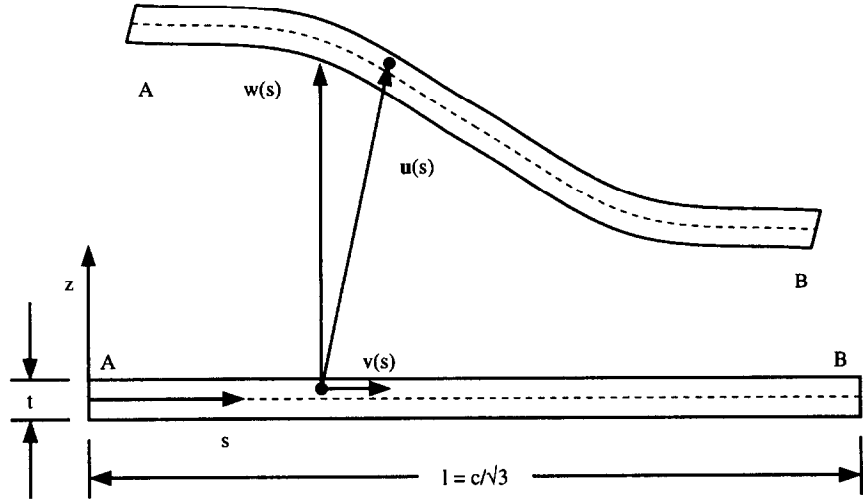

(b)

Fig. 1. The aluminum honeycomb model. (a) Typical planar section of a perfectly periodic honeycomb material, and the corresponding choice for the unit cell. (b) Undeformed and deformed configurations for the honeycomb cell wall beam model, with undeformed length l and thickness t.

Here, the axial strain measure $e(s)$, and the middle line stretch ratio $\lambda(s)$, are expressed in terms of the middle line displacements $v(s)$ and $w(s)$, such that

$$e = \lambda - 1 \quad \text{and} \quad \lambda = [(1+v_{,s})^2 + (w_{,s})^2]^{1/2}, \tag{2}$$

and the bending strain measure $k(s)$ is expressed in terms of the same displacement components, such that

$$k = [(1+v_{,s})w_{,ss} - w_{,s}v_{,ss}]/\lambda^2. \tag{3}$$

The two quantities which are work-conjugate to the previously defined axial strain measure $e(s)$ and bending strain measure $k(s)$, are the axial force $N(s)$ and the bending moment $M(s)$, respectively, which are related to the axial stress $\sigma(s, z)$ by

$$N = \int_{-t/2}^{t/2} \sigma \, dz \quad \text{and} \quad M = \int_{-t/2}^{t/2} \sigma z \, dz. \tag{4}$$

The variational form of the equilibrium equations for the beam, assuming that there are no distributed loads, and under displacement controlled end loading, is given by

$$\int_0^L (N\delta e + M\delta k) \, ds = 0. \tag{5}$$

The pointwise equilibrium equations for the beam are the Euler–Lagrange equations corresponding to eqn (5). A straightforward calculation of these equations, based on the kinematics introduced in eqns (2) and (3), shows that they are identical to the exact equilibrium equations of the beam in the current configuration. This latter set of equations can be derived directly from equilibrium considerations of a beam segment with no distributed load, which is subjected to end axial forces $N(s)$, end shear forces $Q(s)$ (which can be eliminated from the final equilibrium equations), and end bending moments $M(s)$.

It should be emphasized here that the particular choice, made in eqns (2) and (3) for the kinematics of the beam, is what leads to the consistency of the theory; that is, the coincidence of the Euler–Lagrange equations with the exact equilibrium equations of the beam in the current configuration. This consistency is the exception rather than the rule in kinematically nonlinear structural theories of mechanics, in which the adoption of a particular kinematic approximation dictates the form of the Euler–Lagrange equations of the theory, which do not, in general, coincide with the exact equilibrium equations of the structure in the current configuration. In the previously defined sense, consistent, kinematically nonlinear, structural theories exist, only for planar deformations of beams, and axisymmetric deformations of shells. The interested reader is referred to Triantafyllidis and Samanta (1986) for further details.

The last element required to complete the description of the behavior for the cell walls, under general in-plane deformations, is the constitutive law for the honeycomb material. The relationship between the only non-negligible stress component (i.e., the axial stress $\sigma(s, z)$, acting on the cross-section at coordinate s of the beam, at a distance z from the current middle line, in a direction parallel to the middle line), and the corresponding axial strain $\varepsilon(s, z)$, given in eqn (1), is assumed to be a standard bilinear relationship of the form

$$\sigma = \begin{cases} E\varepsilon, & \text{for } \varepsilon \leqslant \varepsilon_y \\ E\varepsilon_y + E_t(\varepsilon - \varepsilon_y), & \text{for } \varepsilon > \varepsilon_y \end{cases}. \tag{6}$$

This relationship was determined by Papka and Kyriakides (1994) to best fit the experimental results, measured from thin strips of aluminum obtained from their

experimentally studied aluminum honeycomb specimens (Aluminum 5052-H39 manufactured by Hexcel Corporation). The stress–strain relationship, given in eqn (6), holds for the case of monotonic loading. In the present formulation, elastic unloading has also been accounted for, by including a kinematic hardening response to eqn (6). It should be emphasized at this point that the proposed general methodology described in this section is independent of the specific form of the constitutive law used to model the material stress–strain response.

Having discussed the modeling of the cell walls, the next issue to be addressed concerns the selection of a "unit cell" for the perfectly periodic honeycomb model. Recall that the unit cell is the fundamental building block of the honeycomb model, and is defined as the smallest representative microsection of the specimen, for which repetitive translation along the coordinate axes (without gap or intersection) reconstitutes the infinite structure. Of the several unit cells that can be selected, the one chosen is shown in Fig. 1(a). This unit cell has initial (i.e., undeformed) dimensions $A_1 = c$ and $A_2 = \sqrt{3}c$, where c is the nominal hexagonal cell size, and $c/\sqrt{3}$ is the length of each cell wall. Due to the manufacturing process, all of the vertical cell walls of the honeycomb have thickness $2t$, while the remaining cell walls have thickness t, where t is the thickness of the aluminum strips that are partially bonded together, and subsequently expanded to produce the honeycomb material. The selection of this particular microsection is motivated by the desire to deal with a unit cell that has only nodes (and no cell walls) on its boundaries. Note also that the unit cell selected has point symmetry with respect to the center node 0.

All of the components are now in place for finding the principal equilibrium solution for the honeycomb model under general in-plane loading. Either the macroscopic deformation gradient components F_{ij}, or their work-conjugate, macroscopic, first Piola–Kirchhoff stress components Π_{ji} can be prescribed. Since, in the applications of interest, the honeycombs are essentially deformed in compression (tensile loadings, in general, result in debonding along the honeycomb walls), attention is focused on macroscopic loadings where both principal macroscopic stresses remain compressive. More specifically, it is assumed that the macroscopic, first Piola–Kirchhoff stress tensor can be decomposed into the following form, which eliminates the arbitrary rigid body rotation in the system:

$$\mathbf{\Pi} = \frac{1}{A_1 A_2}\begin{bmatrix}\cos\theta & -\sin\theta \\ \sin\theta & \cos\theta\end{bmatrix}\begin{bmatrix}\Lambda\cos\phi & 0 \\ 0 & \Lambda\sin\phi\end{bmatrix}\begin{bmatrix}\cos\theta & \sin\theta \\ -\sin\theta & \cos\theta\end{bmatrix}, \tag{7}$$

where $\Pi_1 = \Lambda\cos\phi/A_1A_2$ and $\Pi_2 = \Lambda\sin\phi/A_1A_2$ are the principal macroscopic stresses, and θ is the orientation angle of the principal stress axes with respect to the reference (undeformed) coordinate system (i.e., with respect to the initial axes of material orthotropy).

For the loading conditions considered here, the ratio of the principal macroscopic stresses $\tan\phi$, and the macroscopic load orientation angle θ, are kept fixed. Given that the macroscopic force parameter Λ (which is also a measure of the macroscopic stress amplitude) reaches a maximum for the majority of the load paths considered, the work conjugate quantity Δ, which is found from the requirement that $\Pi_{ji}(F_{ij}-\delta_{ij})A_1A_2h = \Lambda\Delta$, is prescribed instead. Consequently, the dimensionless dis-

placement parameter Δ/h, which is applied to the unit cell, is found from the previous requirement and eqn (7) to be

$$\Delta/h = (\cos^2\theta\cos\phi + \sin^2\theta\sin\phi)(F_{11}-1) + (\sin^2\theta\cos\phi + \cos^2\theta\sin\phi)(F_{22}-1) + \cos\theta\sin\theta(\cos\phi - \sin\phi)(F_{12}+F_{21}). \quad (8)$$

Due to the previously mentioned point symmetry of the unit cell, the principal solution can be found by applying the above prescribed loading to the lower left quarter of the unit cell (the portion of the unit cell bounded by nodes 1, 2, 0, and 3, as shown in Fig. 1(a)). Details concerning the numerical calculations implemented in the solution of the equilibrium equations will be given in Section 3.

2.2. *Onset of failure for infinite honeycombs*

As explained in Section 1, the primary tool used in this investigation to study the onset of failure in honeycomb materials, is the concept of an initial bifurcation surface, which is determined for the corresponding perfectly periodic honeycomb models of infinite extent. The onset of failure surfaces, for the aluminum honeycombs under investigation, are presented in principal macroscopic stress space (Π_1 and Π_2 are the principal values of the macroscopic, first Piola–Kirchhoff stress tensor $\mathbf{\Pi}$, defined in eqn (7)), for different values of the macroscopic load orientation angle θ. These failure surfaces are constructed as follows. Of interest, for each radial load path in principal macroscopic stress space (defined by the load path angle ϕ), is the lowest value of the displacement parameter Δ (defined in eqn (8) as the work-conjugate quantity to the macroscopic force parameter Λ), for which the principal solution for the honeycomb model loses uniqueness. The principal solution in question is the solution for which all unit cells of the honeycomb model deform identically. The values of the principal macroscopic stresses, corresponding to this value of the displacement parameter, can be plotted in macroscopic stress space for each value of the load path angle ϕ, and for a fixed value of the orientation angle θ, to obtain the desired failure surface.

To find the critical displacement parameter Δ_c (and consequently, the critical force parameter Λ_c, and also the critical principal macroscopic stresses Π_1^c and Π_2^c), the uniqueness of the incremental equilibrium solution, for the entire honeycomb model, must be examined for each principal solution along the load path under investigation. Since the principal solution in question is periodic, with the same spatial periodicity as the hexagonal lattice model, the uniqueness of the incremental equilibrium equations for the infinite honeycomb model can be explored by restricting attention to the incremental response of the unit cell. The method used here is based on Bloch wave theory, and has already been described in Triantafyllidis and Schnaidt (1993) for planar frame models. For reasons of completeness, however, a brief description of the method, applied to the honeycomb models, is presented here.

Unlike the principal solution, which due to symmetry arguments (see the discussion at the end of Section 2.1), requires calculations involving only a portion of the unit cell, the stability calculations for the infinite honeycomb model require consideration of the entire microsection (see the definition in Section 2.1). The reason for these considerations can be found in the assumptions made in the Bloch wave theory

representation of the critical bifurcation eigenmode (see eqn (10) below). According to Bloch wave theory, the complete representation of the eigenmode for the infinite honeycomb model is based on the unit cell of the microstructure. For a bifurcated solution to exist, at a given state of deformation for the infinite, perfectly periodic honeycomb model, the incremental force vectors $\dot{\mathbf{f}}_i$, which correspond to the bifurcation eigenmode, and which act on the boundary nodes of each unit cell (i.e., nodes 1–6, shown in Fig. 1(a)), must be related to the corresponding displacement increment vectors $\dot{\mathbf{u}}_j$, by the tangent stiffness matrices $\mathbf{K}_{ij}$:

$$\dot{\mathbf{f}}_i = \sum_{j=1}^{6} \mathbf{K}_{ij} \cdot \dot{\mathbf{u}}_j, \quad i = 1, \ldots, 6. \tag{9}$$

For discrete, periodic systems of infinite extent, it can be shown that, at bifurcation, the eigenmode $\dot{\mathbf{u}}(X_1, X_2)$ can be cast in the following form:

$$\dot{\mathbf{u}}(X_1, X_2) = \exp[i(\omega_1 X_1 + \omega_2 X_2)]\mathbf{p}(X_1, X_2), \tag{10}$$

where ω_1 and ω_2 are the wave numbers of the bifurcation eigenmode along the X_1 and X_2 coordinate directions, respectively, and where $\mathbf{p}(X_1, X_2)$ is a doubly periodic function of the spatial coordinates X_1 and X_2, with fundamental periods equal to the unit cell dimensions (i.e., $\mathbf{p}(X_1 + mA_1, X_2 + nA_2) = \mathbf{p}(X_1, X_2)$ for any pair of integers m and n). Consequently, at bifurcation, the following relations involving the nodal force and displacement increment vectors $\dot{\mathbf{f}}_i$ and $\dot{\mathbf{u}}_i$, at the boundaries of the unit cell, can be deduced from eqn (10):

$$\begin{aligned} &\dot{\mathbf{u}}_6 = \mu_1\mu_2\dot{\mathbf{u}}_1, \quad \dot{\mathbf{u}}_4 = \mu_1\dot{\mathbf{u}}_3, \quad \dot{\mathbf{u}}_5 = \mu_2\dot{\mathbf{u}}_2, \\ &\dot{\mathbf{f}}_6 = \mu_1\mu_2\dot{\mathbf{f}}_1, \quad \dot{\mathbf{f}}_4 = -\mu_1\dot{\mathbf{f}}_3, \quad \dot{\mathbf{f}}_5 = -\mu_2\dot{\mathbf{f}}_2, \end{aligned} \tag{11}$$

where the following definition of the complex coefficients μ_α is introduced (here $i \equiv \sqrt{-1}$):

$$\mu_\alpha \equiv \exp(i\omega_\alpha A_\alpha), \quad \alpha = 1, 2. \tag{12}$$

By introducing relations (11) and definition (12) into the incremental equilibrium eqn (9), one obtains the following equivalent system for the equilibrium of the infinite honeycomb model:

$$\sum_{j=1}^{3} \hat{\mathbf{K}}_{ij} \cdot \dot{\mathbf{u}}_j = 0, \quad i = 1, 2, 3. \tag{13}$$

A nontrivial solution to eqn (13) exists when the matrix $\hat{\mathbf{K}}$ (which is the direct assembly of the submatrices $\hat{\mathbf{K}}_{ij}$) satisfies

$$\det \hat{\mathbf{K}}(\Delta_m, \omega_1 A_1, \omega_2 A_2) = 0. \tag{14}$$

The reduced stiffness matrix $\hat{\mathbf{K}}$ is Hermitian (deduced from the symmetry of $\mathbf{K}$), and depends on the dimensionless wave numbers $\omega_1 A_1$ and $\omega_2 A_2$, as well as on Δ, the displacement parameter of the principal solution. For $\Delta = 0$, the stiffness matrix $\hat{\mathbf{K}}$ is positive definite for all dimensionless wave numbers $\omega_1 A_1$ and $\omega_2 A_2$. As the loading increases, however, one can find, for each fixed pair of wave numbers, a critical

displacement parameter $\Delta_m(\omega_1 A_1, \omega_2 A_2)$ for which eqn (14) is satisfied for the first time. Of interest is the minimum value of the critical displacement parameter Δ_m for all possible wave numbers; that is, for $(\omega_1 A_1, \omega_2 A_2) \in [0, 2\pi) \times [0, 2\pi)$. This minimum value of the critical displacement parameter is denoted by Δ_c.

For each load path through principal macroscopic stress space, that is, for each fixed value of θ and ϕ (see the definitions in eqn (7)), the critical displacement parameter surface, defined by $\Delta_m(\omega_1 A_1, \omega_2 A_2)$, is determined. Two of these surfaces, which are typical for the present investigation, are shown in Fig. 2(a), for $\theta = 0$ and $\tan\phi = 0.839$, and in Fig. 3(a), for $\theta = 0$ and $\tan\phi = 0.700$. Two important remarks, which are applicable, in general, to these surfaces, should be made at this point.

The first remark pertains to the possibility of a singularity existing in the critical displacement parameter surface at the origin of the dimensionless wave number domain; that is, at $(\omega_1 A_1, \omega_2 A_2) = (0, 0)$. Note that two different classes of bifurcation mode shapes are mapped in the neighborhood of the origin. The first class are periodic modes, since the modes corresponding to $\omega_1 A_1 = \omega_2 A_2 = 0$ are spatially periodic, with a wavelength in each coordinate direction which is equal to the dimensions of the unit cell. The second class are long wavelength modes (i.e., modes with wavelengths $L_\alpha \gg A_\alpha$), since the corresponding wave numbers approach zero (i.e., $(\omega_1 A_1, \omega_2 A_2) = (2\pi A_1/L_1, 2\pi A_2/L_2) \to (0, 0)$). The magnified portions of the critical displacement parameter surfaces near the origins of the dimensionless wave number domains are shown in Fig. 2(b) and Fig. 3(b). Notice that the critical displacement parameter surface in Fig. 2 is regular at the origin (i.e., there is no singularity). Moreover, the minimum value of the critical displacement parameter Δ_c is achieved exactly at $(\omega_1 A_1, \omega_2 A_2) = (0, 0)$. This implies that the first bifurcation mode encountered during the biaxial ($\theta = 0$) loading of an infinite honeycomb model with $\tan\phi = 0.839$, is a periodic mode with wavelengths in each coordinate direction which are equal to the unit cell dimensions. In contrast, the critical displacement parameter surface in Fig. 3 is singular at the origin. In addition, the minimum value of the critical displacement parameter is achieved for $(\omega_1 A_1, \omega_2 A_2) \to (0, 0)$, for a fixed ratio $\omega_1 A_1/\omega_2 A_2$. This implies that the first bifurcation mode encountered during the biaxial ($\theta = 0$) loading of an infinite honeycomb model with $\tan\phi = 0.700$, has wavelengths in each coordinate direction that are much larger than the unit cell dimensions. Similar results, concerning the dependence of the critical displacement parameter surface on the dimensionless wave numbers, have already been observed by Triantafyllidis and Schnaidt (1993), for the case of biaxially loaded frame-type models.

The second remark pertains to the symmetries of the critical displacement parameter surface on the dimensionless wave number domain $[0, 2\pi) \times [0, 2\pi)$. Note that, for biaxial loading ($\theta = 0$), the principal solution is symmetric with respect to both the X_1 and X_2 coordinate axes, as well as point symmetric about the center of any unit cell. For the reduced stiffness matrix $\hat{\mathbf{K}}$, defined in eqn (13), these symmetries imply that

$$\begin{aligned}\hat{\mathbf{K}}_{ij}(\Delta, \omega_1 A_1, \omega_2 A_2) &= \hat{\mathbf{K}}_{ij}(\Delta, 2\pi - \omega_1 A_1, \omega_2 A_2) \\ &= \hat{\mathbf{K}}_{ij}(\Delta, \omega_1 A_1, 2\pi - \omega_2 A_2) = \hat{\mathbf{K}}_{ij}(\Delta, 2\pi - \omega_1 A_1, 2\pi - \omega_2 A_2). \quad (15)\end{aligned}$$

For the case of shear loading ($\theta \neq 0$), the principal solution is only point symmetric

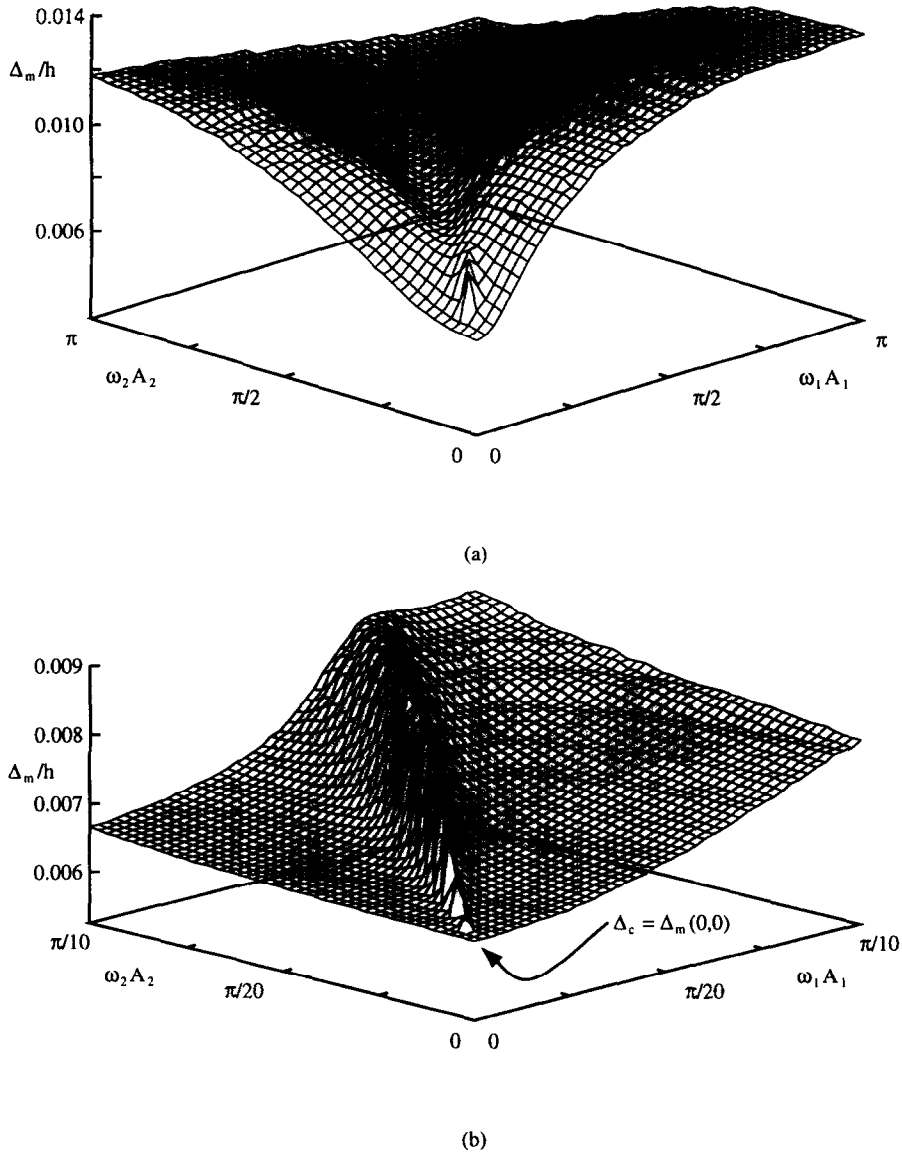

Fig. 2. (a) Critical displacement parameter surface, determined using Bloch wave theory, for an infinite honeycomb model with perfectly periodic microstructure, subjected to biaxial compression along the initial axes of material orthotropy ($\theta = 0$) with $\tan\phi = 0.839$. (b) Magnified portion of the critical displacement parameter surface near the origin of the dimensionless wave number domain (note the minimum exactly at the origin).

about the center of any unit cell. Consequently, the only symmetry exhibited by $\hat{\mathbf{K}}$ in this case is

$$\hat{\mathbf{K}}_{ij}(\Delta, \omega_1 A_1, \omega_2 A_2) = \hat{\mathbf{K}}_{ij}(\Delta, 2\pi - \omega_1 A_1, 2\pi - \omega_2 A_2). \tag{16}$$

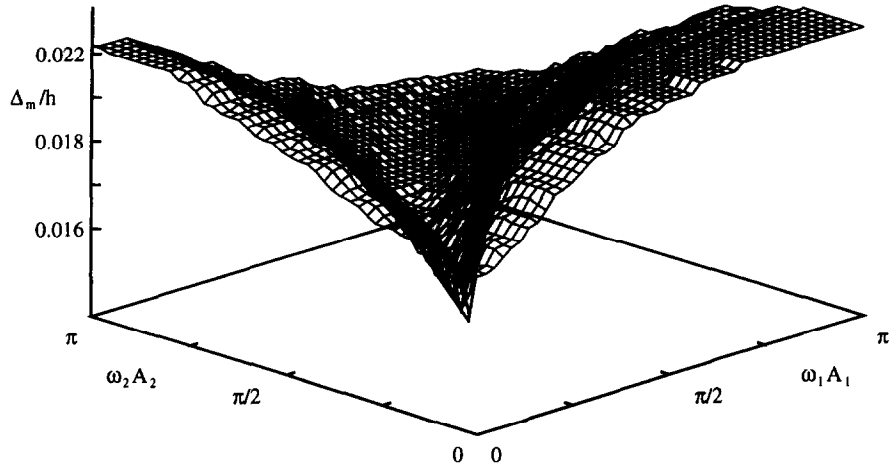

(a)

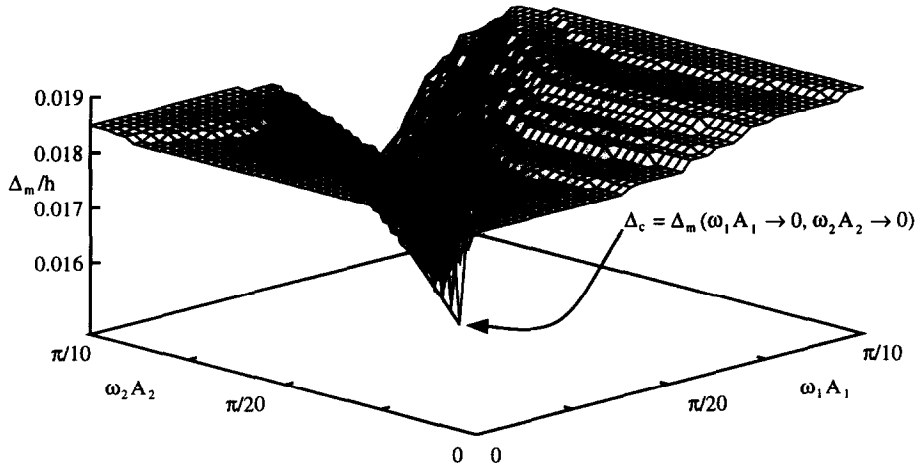

(b)

Fig. 3. (a) Critical displacement parameter surface, determined using Bloch wave theory, for an infinite honeycomb model with perfectly periodic microstructure, subjected to biaxial compression along the initial axes of material orthotropy ($\theta = 0$) with $\tan\phi = 0.700$. (b) Magnified portion of the critical displacement parameter surface near the origin of the dimensionless wave number domain (note the singularity at the origin).

The symmetries of the reduced stiffness matrix for the infinite honeycomb model reduce the computational time required to find the critical displacement parameter surfaces (i.e., the surfaces defined by $\Delta_m(\omega_1 A_1, \omega_2 A_2)$). Hence, for $\theta = 0$, only one quarter of the full dimensionless wave number domain $[0, 2\pi) \times [0, 2\pi)$ needs to be

surveyed (this explains why the critical displacement parameter surfaces in Fig. 2(a) and Fig. 3(a) are plotted in the domain $[0, \pi] \times [0, \pi]$), while for $\theta \neq 0$, half of the full dimensionless wave number domain needs to be examined.

Having discussed the theoretical modeling issues for this problem, the numerical algorithms used for their solution, along with the main results of this investigation, can now be presented in the next section.

3. RESULTS AND DISCUSSION

Although the methodology proposed in Section 2 is applicable to honeycombs made of any rate-independent material (elastic or elasto-plastic), the numerical applications presented here are calculated for the aluminum (Aluminum 5052-H39) honeycomb specimens used in the experimental investigations of Papka and Kyriakides (1994). Unless otherwise stated, the nominal cell size is $c = 9.53$ mm, and the cell wall thickness is $t = 0.145$ mm. The experimentally determined parameters, required in eqn (6) for the description of the uniaxial stress–strain response of the honeycomb cell walls, are: Young's modulus $E = 69$ GPa, yield strain $\varepsilon_y = 4.23 \times 10^{-3}$, and tangent modulus $E_t = E/100$.

Following a description of the numerical algorithm used in the present calculations, the principal solutions for the infinite honeycomb models, as well as the corresponding onset of plasticity and maximum load surfaces, are discussed under the conditions of general in-plane loading. Next, the initial bifurcation surfaces for the infinite honeycomb models are examined, followed by an investigation of the geometric scale effects on these failure surfaces. Finally, the influence of microstructural imperfections on the initial bifurcation surfaces of the honeycomb models are explored.

3.1. *Description of numerical algorithm*

A finite element discretization of the governing eqns (1)–(6) is the basis for the numerical calculations presently reported. Each cell wall is divided into ten elements of equal length $l_e = c/10\sqrt{3}$. Within each element, a Hermitian cubic interpolation scheme has been adopted for the displacements $v(s)$ and $w(s)$. Consequently, the degrees of freedom, at a node with coordinate s_i along the length of the element, are $\mathbf{u}_i = (v(s_i), w(s_i), v_{,s}(s_i), w_{,s}(s_i))$. A four point Gaussian quadrature is employed for the numerical integration along the beam element length, while a straightforward trapezoid rule using 81 points is employed for the numerical integration through the thickness of the beam. This, perhaps excessive, accuracy was adopted to capture the exact location of the elastic–plastic boundary, in view of the sharp discontinuity present in the uniaxial stress–strain response.

The continuity conditions at the vertices of the hexagonal cells (i.e., the nodes where the cell walls connect) merit a short discussion, due to the adoption of a simplifying assumption. At each vertex, the continuity of the nodal displacement vector must be ensured. This implies that the first two components, that is, v and w, of the vertex degrees of freedom (expressed in the global coordinate system), are the

same for the end nodes of each of the three elements connected at the vertex under consideration. Moreover, the rigidity of the vertex connection dictates that each of the three elements must rotate by the same angle $\alpha = \arctan[w_{,s}/(1+v_{,s})]$, where $v_{,s}$ and $w_{,s}$ are expressed in the local coordinate system of each element connected at that vertex. From the adopted kinematics, it can be shown that $\cos\alpha = (1+v_{,s})/\lambda$ and $\sin\alpha = w_{,s}/\lambda$. By assuming that at each vertex $\lambda \approx 1$, it can be shown that $v_{,s}$ and $w_{,s}$ (expressed in the local coordinate system of each element) have to be the same for the end nodes of each of the elements connected at the vertex in question. This assumption, which is based on the observation that, under compressive macroscopic stresses, the honeycomb specimens deform essentially through bending of the cell walls, was verified and found to be true for all of the numerical calculations reported here.

For the principal solution, only one quarter of the unit cell (the portion of the unit cell bounded by nodes 1, 2, 0, and 3, as shown in Fig. 1(a)) is considered. An incremental Newton–Raphson solution procedure is employed to determine the solution to the problem. Periodicity conditions dictate that the moment at each boundary node vanishes, and hence, one need only impose displacements v and w, at each boundary node, which are compatible with the macroscopic deformation gradient $\mathbf{F}$. A typical increment size for the nondimensional displacement parameter Δ/h, used in the solution of the equilibrium equations, is 5×10^{-4}.

To construct the initial bifurcation surfaces for the infinite honeycomb models, the entire unit cell (i.e., the unit cell with end nodes 1, 3, 5, 6, 4, and 2, as shown in Fig. 1(a)) is considered. The real, 24×24 stiffness matrix $\mathbf{K}$ for the unit cell, is obtained by static condensation of the non-boundary degrees of freedom. Further condensation using the relations (11) and definition (12), results in a reduced, 12×12, Hermitian stiffness matrix $\hat{\mathbf{K}}(\Delta, \omega_1 A_1, \omega_2 A_2)$. The Choleski decomposition of $\hat{\mathbf{K}}(\Delta, \omega_1 A_1, \omega_2 A_2)$, used in the numerical solution of the incremental equilibrium equations, provides a real, diagonal matrix $\mathbf{D}$. As the displacement parameter Δ increases from zero, the reduced stiffness matrix $\hat{\mathbf{K}}(\Delta, \omega_1 A_1, \omega_2 A_2)$ loses, for the first time, its positive definiteness, for some value of the displacement parameter, denoted by Δ_m. Consequently, the minimum entry of the diagonal matrix $\mathbf{D}$ changes sign at this stage of loading. To find the critical displacement parameter surface (i.e., the surface defined by $\Delta_m(\omega_1 A_1, \omega_2 A_2)$) corresponding to each load path in principal macroscopic stress space (i.e., for fixed values of θ and ϕ), the dimensionless wave number domain is typically covered with a uniformly spaced grid, for which the wave number increments are $\delta(\omega_1 A_1) = \delta(\omega_2 A_2) = \pi/180$. A much denser grid with $\delta(\omega_1 A_1) = \delta(\omega_2 A_2) = \pi/18{,}000$ is employed near the origin of the dimensionless wave number domain, in order to accurately capture any long wavelength bifurcation modes.

For the case of finite sized honeycomb models, a straightforward incremental Newton–Raphson solution procedure is employed to find the equilibrium solution of the entire specimen. To reduce the size of the final stiffness matrix, static condensation is used to create a superelement for each half cell wall. The stability for each of the finite honeycomb models is investigated by examining the loss of positive definiteness of the resulting incremental stiffness matrix. This is accomplished, again, using the criterion of sign change in the minimum entry of the diagonal matrix $\mathbf{D}$, found through Choleski decomposition of the final stiffness matrix in question.

A number of nontrivial model verifications have been employed to check the accuracy of this numerical algorithm. These verifications range from analytical solutions developed for certain deformations of the cell walls, to a comparison of the results, determined for the case of uniaxial compression, with the results given by Papka and Kyriakides (1994) for a similar microsection.

Finally, some comments concerning the magnitude of the axial strains in the cell wall elements, and the possibility of reloading during the finite deformations, are in order. The maximum axial strain over all of the elements of the model is identified in each numerical calculation. Given the fact that the applied principal macroscopic stresses are compressive, the honeycomb deforms essentially through bending of the cell walls. Consequently, the absolute value of the maximum axial strain is never found to exceed 0.01 (recall that to ensure continuity of the displacement vector at each hexagon vertex, $\lambda \approx 1$, or $e \approx 0$). As far as unloading is concerned, it has been observed that, in general, immediately following a maximum load, the stresses in some elements decrease. Since, in this investigation, deformations approaching complete collapse of the honeycomb models are never attained (i.e., no contact of the cell walls occurs in these calculations), reloading has never been observed, thus making moot the distinction between isotropic hardening and the kinematic hardening model adopted.

3.2. *Onset of plasticity and maximum load*

As previously discussed, the principal solution for the finite honeycomb model is obtained by applying the macroscopic stress state, defined in eqn (7), to the unit cell. This is accomplished by prescribing the displacement parameter Δ, which is the work-conjugate displacement to the force parameter Λ, for a fixed ratio and orientation of the principal macroscopic stresses. Some typical force–displacement responses, for the perfectly periodic aluminum honeycombs under investigation, are shown in Fig. 4(a). More specifically, the dimensionless force parameter, Λ/EA_1A_2, is plotted versus the dimensionless displacement parameter Δ/h, for a fixed principal stress ratio $\tan\phi = 2.747$, and for three different values of the macroscopic load orientation angle θ. For each force-displacement response, the onset of plasticity (i.e., the instance for which the outer fiber of a cell wall reaches the yield stress σ_y) is denoted by ($\square$), the maximum load is denoted by ($\triangle$), and the initial bifurcation in the principal equilibrium solution of the infinite honeycomb model is denoted by ($\bigcirc$).

By scanning over all values of the load path angle ϕ between π and $3\pi/2$ (while keeping the orientation angle θ constant), the onset of plasticity surface and the maximum load surface can be plotted in principal macroscopic stress space. The onset of plasticity surface (depicted by the solid line) and the maximum load surface (depicted by the dotted line) are shown for the case of biaxial compression along the initial axes of material orthotropy ($\theta = 0$) in Fig. 5(a), and for the case when the principal stress state is oriented at $\theta = \pi/4$ with respect to these axes in Fig. 5(b). The shape of both surfaces is similar, and as is expected by their respective definitions, the onset of plasticity surface is completely contained within the maximum load surface. In both figures the onset of plasticity and maximum load surfaces are plotted for a range of principal macroscopic stresses between 0 MPa and -0.4 MPa. This particular

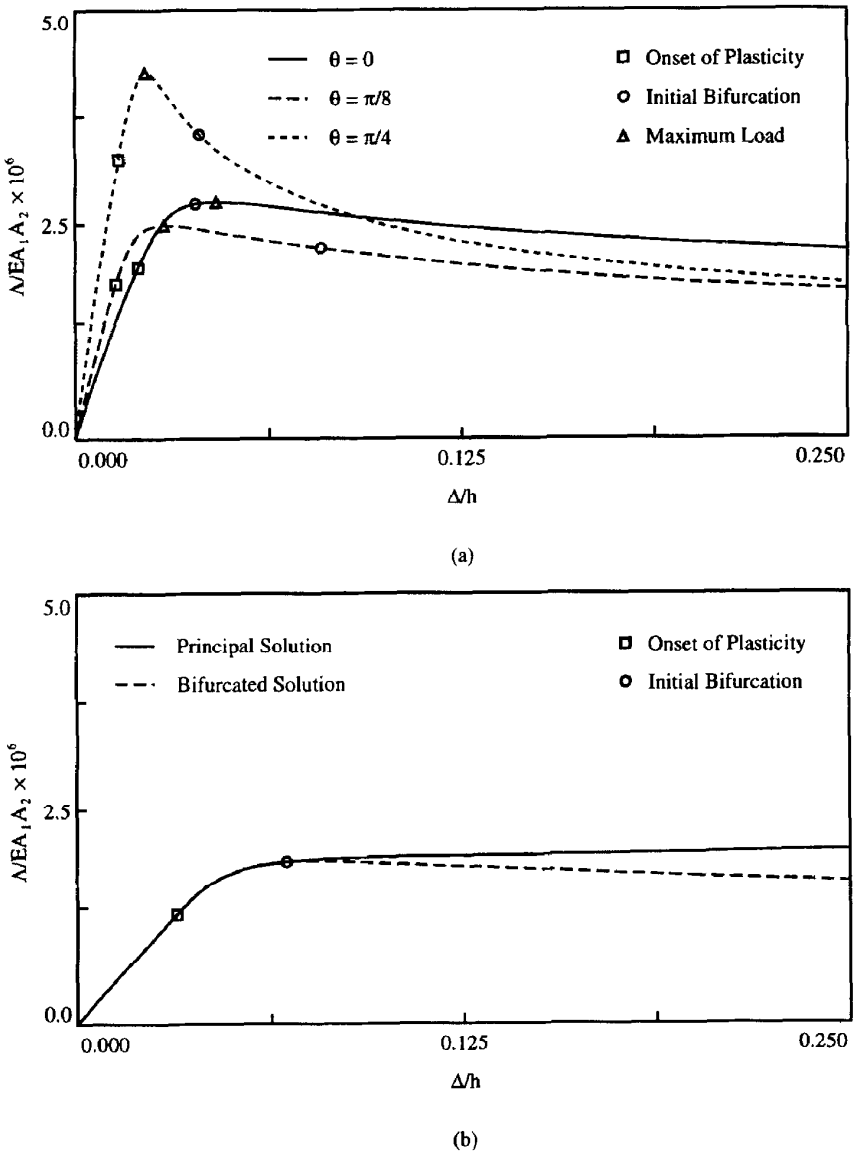

Fig. 4. (a) Typical dimensionless force-displacement response for an infinite honeycomb model with perfectly periodic microstructure, subjected to biaxial compression oriented at three different angles to the initial axes of material orthotropy with $\tan\phi = 2.747$. (b) Corresponding dimensionless force-displacement response (principal and bifurcated solutions) for biaxial compression along the axes of orthotropy ($\theta = 0$) with $\tan\phi = \infty$.

region of macroscopic stress space is chosen in anticipation of the initial bifurcation surface, which is entirely contained within this range.

For the case of balanced biaxial compression (i.e., for the case when $\Pi_1 = \Pi_2$), all cell walls are under the same axial force, and therefore, deform only in the axial

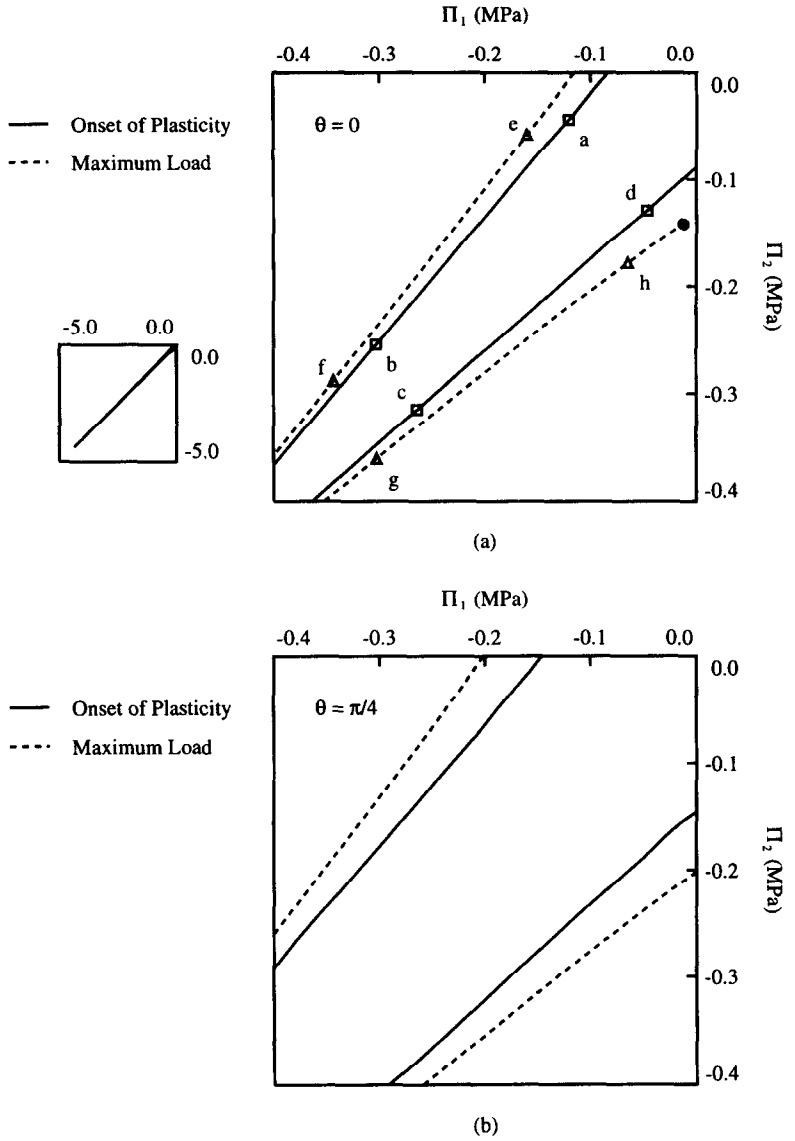

Fig. 5. Onset of plasticity and maximum load surfaces in principal macroscopic stress space for an infinite honeycomb model with perfectly periodic microstructure, subjected to (a) biaxial compression along the initial axes of material orthotropy ($\theta = 0$) and (b) biaxial compression oriented at $\theta = \pi/4$ to the axes of orthotropy.

direction. Due to the absence of bending, the principal macroscopic stresses at the onset of plasticity, and at maximum load, attain their highest possible values for this particular load path (the principal stresses are approximately -4.2 MPa and -4.5 MPa at the onset of plasticity and at the maximum load, respectively). As a result, the complete onset of plasticity and maximum load surfaces are extremely

narrow, and can be approximated by simply extrapolating the failure surfaces shown in Fig. 5(a) and Fig. 5(b). The failure surfaces in question are shown in their entirety in the inset of Fig. 5(a), for the case of biaxial compression along the initial axes of material orthotropy ($\theta = 0$).

For the principal macroscopic stress range of interest (i.e., the range between 0 MPa and -0.4 MPa) it can be seen that the domain of stress space corresponding to completely elastic deformation, and the domain of stress space corresponding to deformations occurring prior to maximum load, are much larger when the principal stresses are oriented at $\theta = \pi/4$ to the initial axes of material orthotropy, as shown in Fig. 5(b), than the corresponding domains resulting for biaxial compression along these axes ($\theta = 0$), as shown in Fig. 5(a). The reason for this difference is illustrated in Fig. 4(a), which shows significant increases in the load levels corresponding to the onset of plasticity and the maximum load, between two typical force-displacement curves: the first, for the case when $\theta = 0$, and the second, for the case when $\theta = \pi/4$. Notice, however, that the increases in the maximum load levels are not monotonic functions of the macroscopic load orientation angle θ, as one can also see in Fig. 4(a) (note the decrease in the load levels for the case when $\theta = \pi/8$).

An important observation to be made from the results presented in Fig. 5, is that a maximum load is reached for all load paths with a macroscopic load orientation angle of $\theta = \pi/4$, while for $\theta = 0$, a maximum load does not exist for a range of deformations near the load path corresponding to uniaxial compression in the vertical direction (i.e., the load path for which $\Pi_1 = 0$ and $\Pi_2 < 0$). The maximum load surface terminates at the point denoted by (•), near the Π_2 axis. For this particular case of uniaxial compression ($\theta = 0$ and $\phi = \infty$), the force-displacement response shown in Fig. 4(b) exhibits no maximum load, but shows a very slight load increase for $\Delta/h > 0.065$. The results for this particular load path, which correspond to the experimental results of Papka and Kyriakides (1994), constitute a singular exception among all of the load paths considered in this investigation.

Finally, of additional interest, is the shape of the onset of plasticity and maximum load surfaces in macroscopic strain space. Both of these surfaces, which were depicted in principal macroscopic stress space in Fig. 5(a) for $\theta = 0$, are plotted in principal macroscopic strain space in Fig. 6 (since $\theta = 0$, $\Pi_{12} = \Pi_{21} = 0$ and $F_{12} = F_{21} = 0$, and therefore, the only non-zero components of the deformation gradient tensor are F_{11} and F_{22}, which are work conjugate quantities to the non-zero components of the macroscopic, first Piola–Kirchhoff stress tensor Π_{11} and Π_{22}, respectively). The hatched area in Fig. 6 corresponds to load paths for which at least one principal macroscopic stress component is in the tensile range. The thin slivers between this hatched area, which are bounded by the onset of plasticity surface (depicted by the solid line) and the maximum load surface (depicted by the dotted line), are the domains of strain space corresponding to completely elastic deformation, and deformations occurring prior to maximum load, respectively. As one can see by the points marked *a* through *h* in Fig. 6(a), and the magnified portion of the failure surfaces shown in Fig. 6(b), there can be a dramatic change in the macroscopic stress state at the onset of plasticity, and at the maximum load, for an extremely small change in the corresponding macroscopic strain rate (compare these points, and their relative proximity, to the corresponding points in principal macroscopic stress space, as shown in Fig. 5). This extreme sensitivity of the onset of plasticity and the maximum

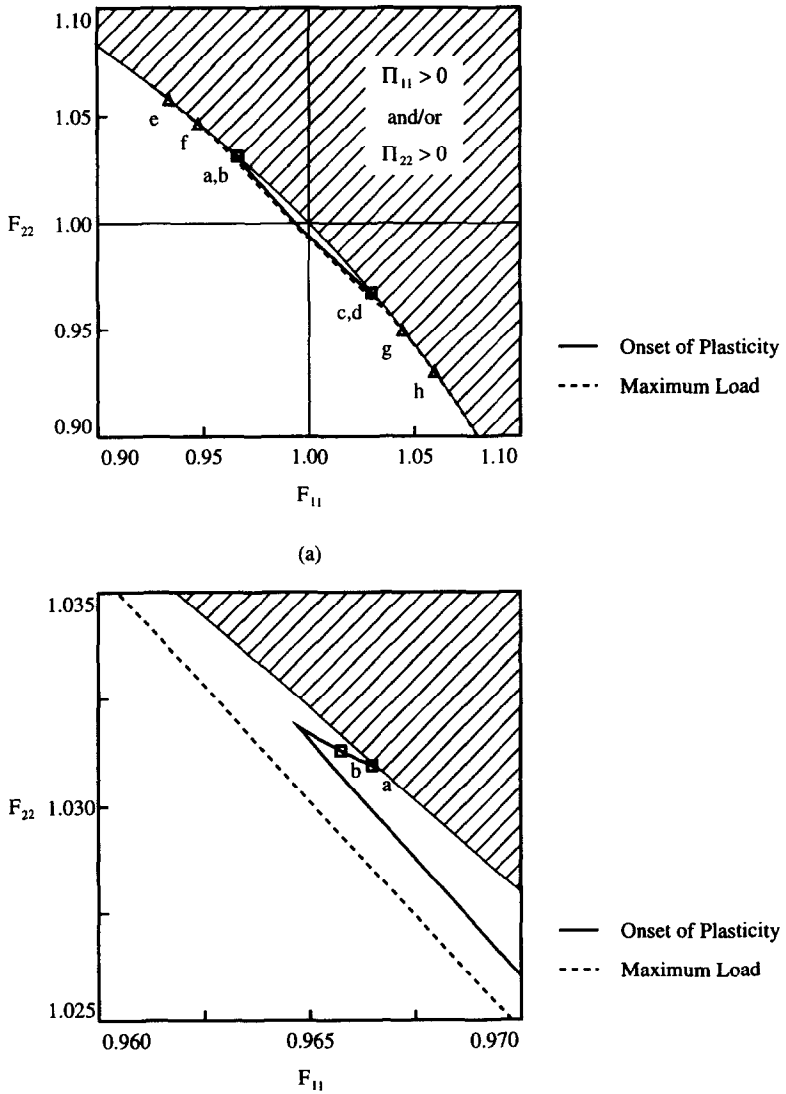

Fig. 6. (a) Onset of plasticity and maximum load surfaces in principal macroscopic strain space for an infinite honeycomb model with perfectly periodic microstructure, subjected to biaxial compression along the initial axes of material orthotropy ($\theta = 0$). (b) Magnified portion of the failure surfaces. Note the extreme sensitivity of the macroscopic stress state at failure to small changes in the load path angle (compare to the previous figure).

load surfaces to small variations in the load path, is the primary reason for presenting the results of this investigation in principal macroscopic stress space.

3.3. *Initial bifurcation*

Having constructed the onset of plasticity and the maximum load surfaces for the perfectly periodic honeycomb model, attention is focused next on the calculation of

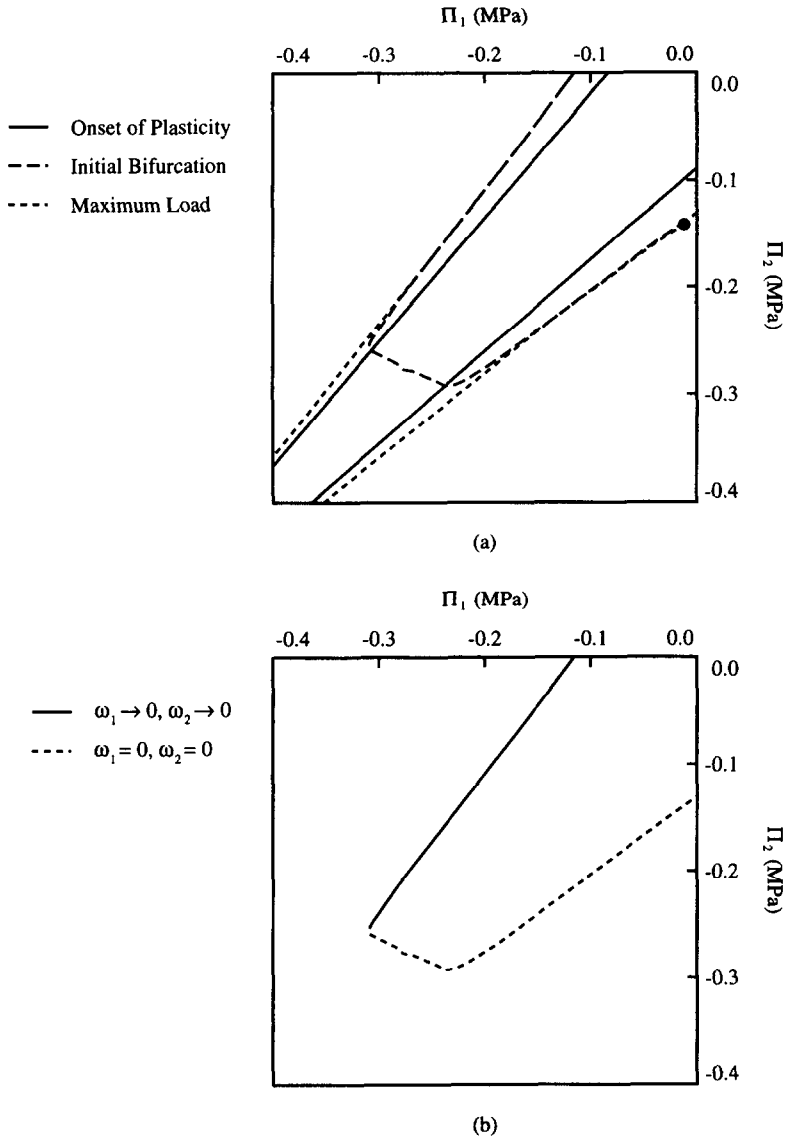

Fig. 7. (a) Onset of plasticity, initial bifurcation, and maximum load surfaces in principal macroscopic stress space for an infinite honeycomb model with perfectly periodic microstructure, subjected to biaxial compression along the initial axes of material orthotropy ($\theta = 0$). (b) Regions of the initial bifurcation surface corresponding to the two different bifurcation mode shapes.

the initial bifurcation surface. By definition, in principal macroscopic stress space, the initial bifurcation surface must be contained within the maximum load surface, as seen in Fig. 7(a) for an infinite honeycomb model subjected to biaxial compression along the initial axes of material orthotropy ($\theta = 0$), and in Fig. 8(a) for the same model subjected to biaxial compression oriented at $\theta = \pi/4$ to these axes.

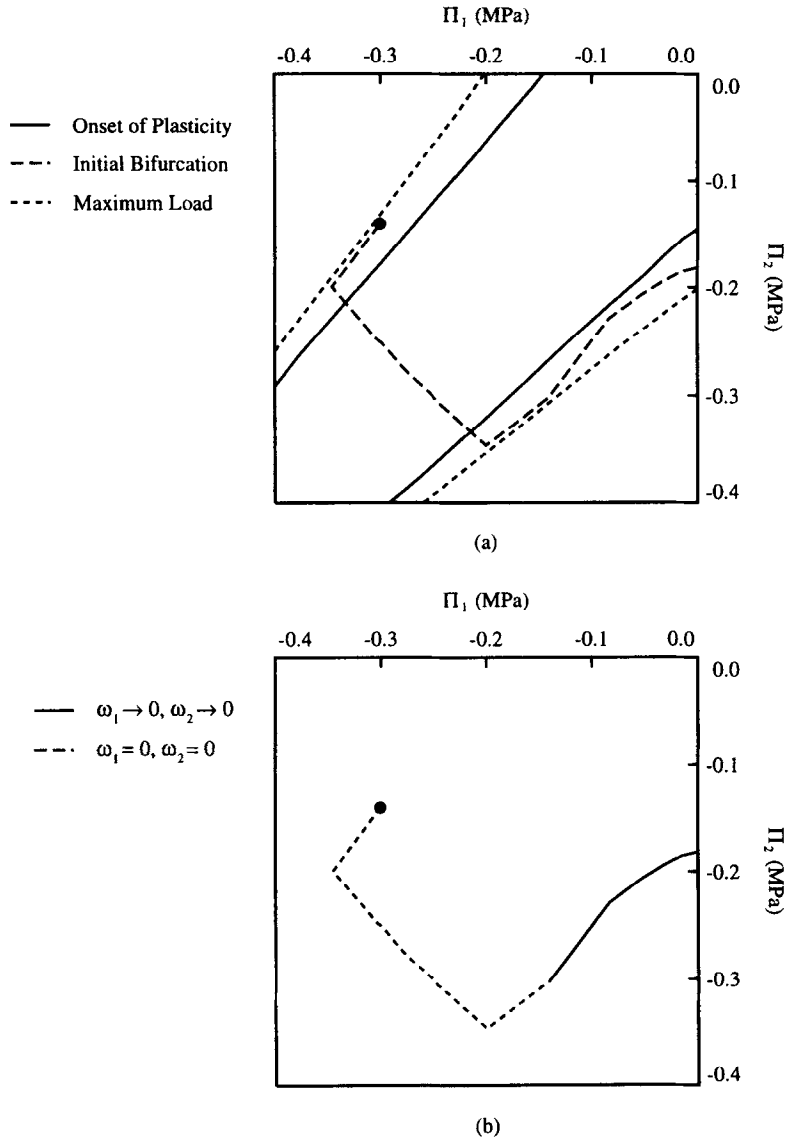

Fig. 8. (a) Onset of plasticity, initial bifurcation, and maximum load surfaces in principal macroscopic stress space for an infinite honeycomb model with perfectly periodic microstructure, subjected to biaxial compression oriented at $\theta = \pi/4$ to the initial axes of material orthotropy. (b) Regions of the initial bifurcation surface corresponding to the two different bifurcation mode shapes.

More specifically, Fig. 7(a) depicts, in principal macroscopic stress space, the initial bifurcation surface for an infinite honeycomb model, and shows the relative position of this surface with respect to the onset of plasticity and maximum load surfaces. Note that the initial bifurcation surface differs significantly from the onset of plasticity and the maximum load surfaces for stress states near the balanced biaxial compression

range (i.e., for stress states in which $\Pi_1 \approx \Pi_2$). In these situations, the initial bifurcation surface is mainly within the elastic domain of the honeycomb material response. For load paths with an adequate deviation from the balanced biaxial compression range, however, the initial bifurcation surface becomes almost indistinguishable from the maximum load surface, as shown in Fig. 7(a).

Another important issue concerns the type of eigenmode that results from the initial bifurcation in the principal equilibrium solution. For all of the load paths considered, the minimum value of the critical displacement parameter (i.e., $\Delta_c = \min \Delta_m(\omega_1 A_1, \omega_2 A_2)$) always occurs at the origin of the dimensionless wave number domain. The portion of the initial bifurcation surface for which the corresponding modes are periodic, with wavelengths in each coordinate direction which are equal to the unit cell dimensions (i.e., the portion for which the surfaces defined by $\Delta_m(\omega_1 A_1, \omega_2 A_2)$ are regular at the origin, with the minimum critical displacement parameter occurring at $\omega_1 A_1 = \omega_2 A_2 = 0$, as shown, for example, in Fig. 2), is plotted in Fig. 7(b) with a dotted line. Alternatively, the portion of the surface for which the corresponding modes are long wavelength modes (i.e., the portion for which the surfaces defined by $\Delta_m(\omega_1 A_1, \omega_2 A_2)$ are singular at the origin, with the minimum critical displacement parameter occurring at $\omega_1 A_1 \to 0$ and $\omega_2 A_2 \to 0$, as shown, for example, in Fig. 3), is plotted in Fig. 7(b) with a solid line.

Notice in Fig. 7(a) that in the case for which the principal axes of stress are aligned with the initial axes of orthotropy of the honeycomb material ($\theta = 0$), the principal solution for the infinite honeycomb model reaches a bifurcation point for all load paths through principal macroscopic stress space (i.e., for all values of the load path angle ϕ). Moreover, the initial bifurcation always occurs prior to the maximum load (assuming that the maximum load exists), as seen in the two examples plotted with solid lines in Fig. 4.

The results depicted in Fig. 8(a) and Fig. 8(b) are analogous to their counterparts presented in Fig. 7(a) and Fig. 7(b), respectively, but correspond to a principal stress state oriented at $\theta = \pi/4$ with respect to the initial axes of orthotropy of the honeycomb material. The main difference between these two cases is that, for $\theta = \pi/4$, a maximum load is reached for all load path angles ϕ (compare Fig. 8(a) to Fig. 7(a)), while no bifurcation in the principal solution is found for a large range of the load path angle (compare Fig. 8(b) to Fig. 7(b)). Moreover, the initial bifurcation for these load paths can occur after the maximum load, as seen by the examples plotted with dashed and dotted lines in Fig. 4(a).

The fact that the initial bifurcation surface, when depicted in principal macroscopic stress space, is, by definition, contained within the maximum load surface, can be misleading, since it does not necessarily imply that a bifurcated solution precedes the maximum load. To better illustrate this idea, the dependence of the displacement parameter Δ, on the load path angle ϕ, at the onset of plasticity, at the initial bifurcation in the principal solution, and at the maximum load, is plotted in Fig. 9(a), for an infinite honeycomb model, subjected to biaxial compression along the initial axes of material orthotropy ($\theta = 0$), and in Fig. 9(b) for an infinite model subjected to biaxial compression oriented at $\theta = \pi/4$ to these axes. These figures show that the initial bifurcation in the principal solution always occurs prior to the maximum load for $\theta = 0$ (see Fig. 9(a)), while for $\theta \neq 0$ the first bifurcation can occur well after the force parameter Λ has reached a maximum value, as seen in Fig. 9(b) for values of ϕ greater than approximately $4\pi/3$.

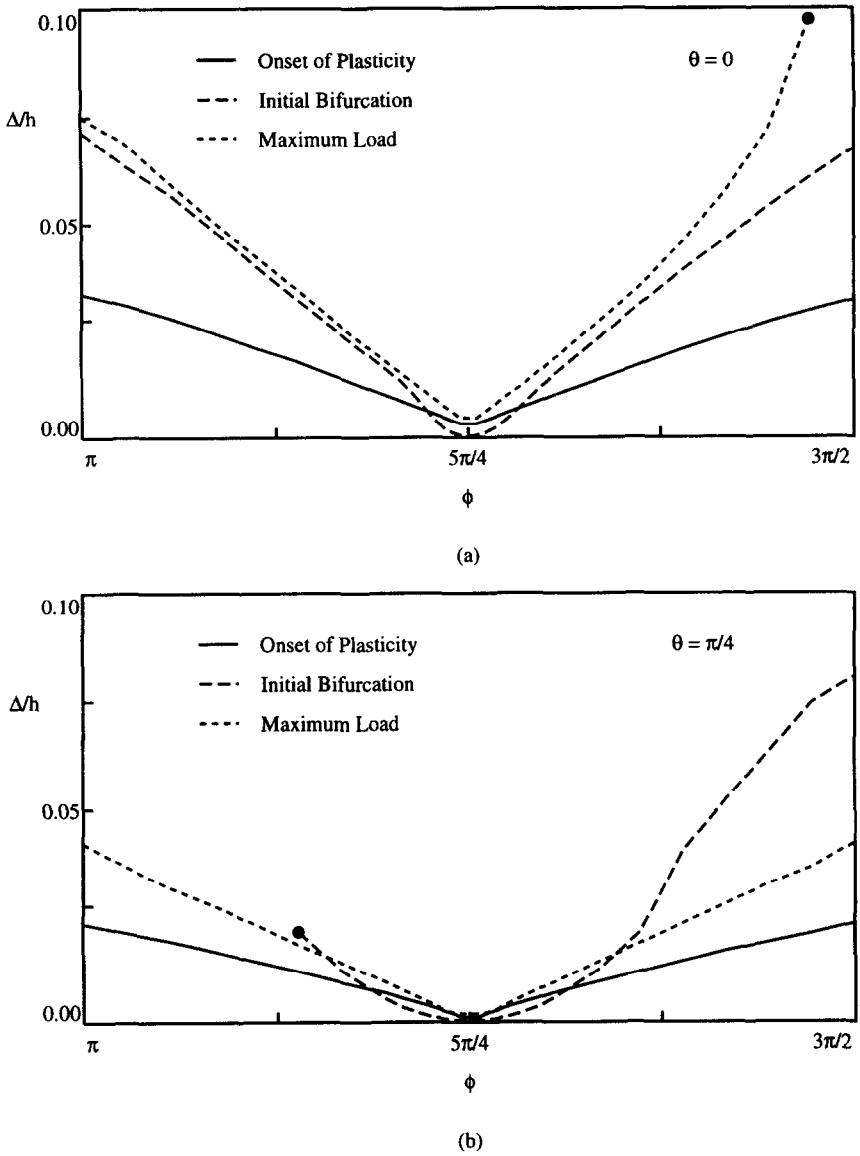

Fig. 9. Value of the dimensionless displacement parameter Δ/h at the onset of plasticity, the initial bifurcation in the principal equilibrium solution, and the maximum load, as a function of the load path angle ϕ for (a) biaxial compression along the initial axes of material orthotropy ($\theta = 0$), and (b) biaxial compression oriented at $\theta = \pi/4$ to the axes of orthotropy.

3.4. *Effects of varying wall thickness*

Honeycomb materials are typically manufactured by bonding strips of material together, and then expanding the ensemble into the proper configuration. Strips of varying thickness can be used to produce honeycombs with specific mechanical

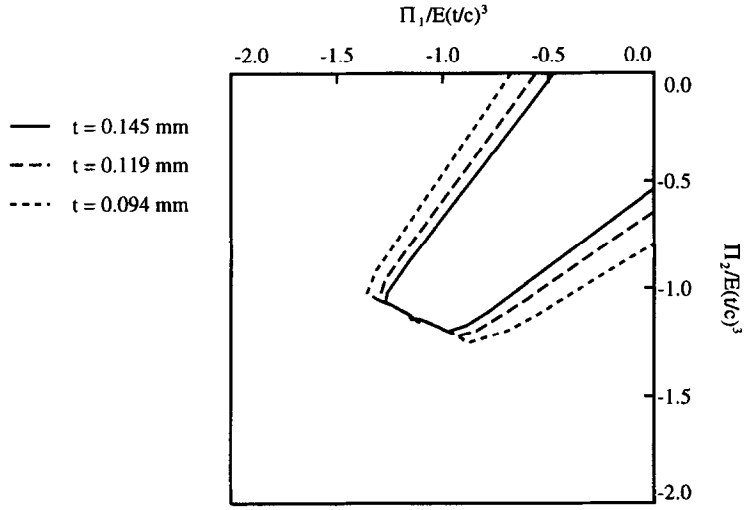

Fig. 10. Effects of varying honeycomb cell wall thickness on the initial bifurcation surface for an infinite honeycomb model with perfectly periodic microstructure, subjected to biaxial compression along the initial axes of material orthotropy ($\theta = 0$).

properties. Given that the stresses, at the initial bifurcation in the principal equilibrium solution for these materials, depend on the bending stiffness of the cell walls, it seems reasonable to expect that the corresponding failure surfaces should be scaled with the cube of the cell wall thickness.

The results in Fig. 10, which correspond to the case of biaxial compression along the axes of orthotropy of the honeycomb material ($\theta = 0$), show the initial bifurcation surfaces for honeycomb models with three different values of the cell wall thickness. These models correspond to the honeycomb specimens investigated experimentally by Papka and Kyriakides (1994). Since the macroscopic elastic moduli of the honeycomb materials are proportional to the parameter $E(t/c)^3$ (see Gibson and Ashby, 1988), the principal macroscopic stresses, plotted in Fig. 10, are nondimensionalized accordingly. Notice that the portions of the initial bifurcation surfaces, which are contained in the completely elastic domain of deformation, coincide for the three different honeycomb models. This result comes as no surprise, since the principal solutions for balanced biaxial compressive loading do not involve any significant bending of the honeycomb cell walls. Consequently, the corresponding bifurcation is due to the elastic buckling of the (nearly) straight, prestressed cell walls, in which case the critical stresses are proportional to the elastic bending stiffness of these walls.

For the portions of the initial bifurcation surfaces which are contained in the plastic domain, however, the initial bifurcations for the honeycombs with the thinner cell walls appear at higher levels of this nondimensionalized stress. This is due to the adopted stress parameterizations, and explains the apparent stiffening of the honeycombs with the thinner cell walls, which bifurcate in the plastic range of deformation. These results are in agreement with the experimental findings of Papka and Kyriakides, for the case of uniaxial compression in the vertical direction (see Fig. 12 in Papka and Kyriakides, 1994).

3.5. *Geometric scale effects*

The results presented thus far have been obtained for the infinite honeycomb model with a perfectly periodic, lattice geometry. Since engineering applications involve the use of finite specimens, which invariably possess imperfections in the geometries of the underlying microstructures, the remainder of this presentation is devoted to an investigation of the geometric scale effects, and the influence of microstructural imperfections, on the onset of failure in aluminum honeycombs.

A typical, finite honeycomb specimen, with perfectly periodic microstructure, together with the corresponding applied loading conditions, is shown in Fig. 11(a). The model comprised of $m \times n$ hexagonal cells, and configured as shown in Fig. 11, has overall dimensions $L_1 = mA_1$ and $L_2 = (n+1/3)(A_2/2)$. The forces applied on the boundary of the specimen are given by $F_1 = \Pi_1 L_2 h$ and $F_2 = \Pi_2 L_1 h$, where the principal macroscopic stresses Π_1 and Π_2 are given by eqn (7). The prescribed quantities for these analyses are the load path angle ϕ (which dictates the ratio of the principal macroscopic stresses), and the displacement parameter Δ, obtained from eqn (8) by setting the macroscopic load orientation angle θ equal to zero. The particular form of the boundary geometry, for the finite specimen, coincides with that which was used in the experimental investigations of Papka and Kyriakides (1994).

Three different finite honeycomb models are studied, each model being comprised of $n \times n$ hexagonal cells, where $n = 3$, 9, and 15, respectively. For these specimens, the geometric scale parameter is defined as $\varepsilon \equiv 1/n$. As discussed in Section 3.1, the initial bifurcation instabilities for the finite honeycomb models occur at the first loss of positive definiteness in the corresponding incremental stiffness matrices. The results of the numerical calculations, used to determine the location of these bifurcation instabilities, are shown in Fig. 12, in which, for purposes of comparison, the initial bifurcation surface for the corresponding infinite honeycomb model (i.e., the model for which $\varepsilon \to 0$) has also been plotted (the failure surface of the infinite model is depicted by the solid line). As expected, the initial bifurcation surfaces for the finite specimens converge to the corresponding failure surface of the infinite honeycomb model, as the geometric scale parameter approaches zero. What is possibly more interesting, is that this convergence is not monotonic, due to boundary effects, as one can see by examining the results for the smaller specimen (i.e., the results for $\varepsilon = 0.333$), shown in Fig. 12.

Notice that the onset of failure surfaces differ substantially in the elastic domain of response, yet are almost coincident for deformations in the plastic domain. To understand this behavior, recall from Fig. 7(a) the close proximity between the initial bifurcation surface and the maximum load surface, as presented in principal macroscopic stress space, for the infinite honeycomb model. Since the principal solutions for the finite honeycombs are almost identical to the corresponding principal solutions for the infinite models, this proximity of the initial bifurcation surfaces for the finite honeycombs, in the plastic region of deformation, comes as no surprise.

Additional information about the nature of the eigenmode at the onset of failure (i.e., whether the instability mode is local or global in nature), for the finite honeycomb models with perfectly periodic microstructures, can be obtained from information about the dimensionless wave numbers at criticality, for the corresponding honey-

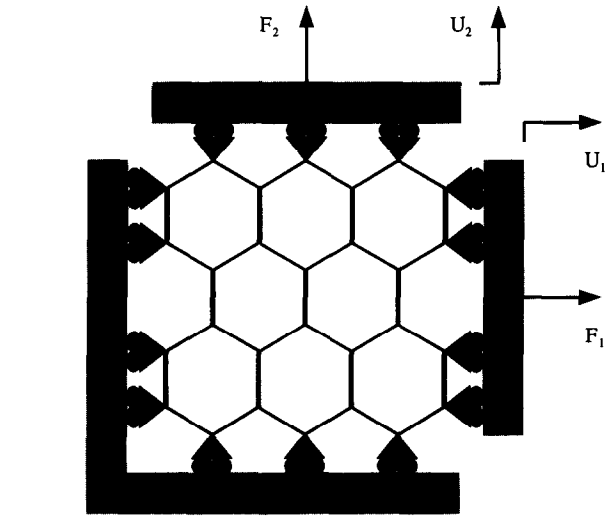

(a)

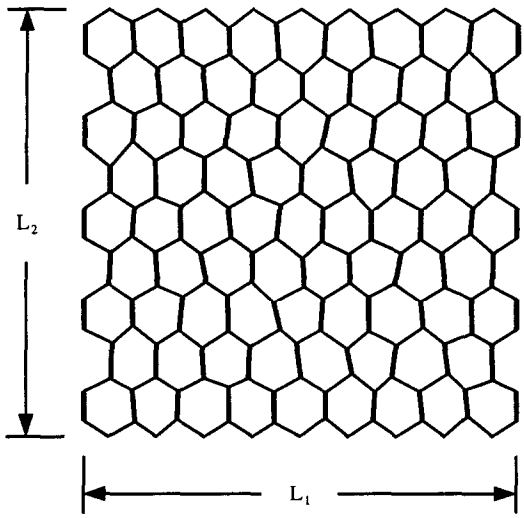

(b)

Fig. 11. (a) Typical finite honeycomb model with perfectly periodic microstructure, and the corresponding applied loading conditions. (b) Finite honeycomb model with random geometric imperfections in the material microstructure.

comb model of infinite extent. The eigenmodes shown in Figs 13(a,b) have been determined for a finite honeycomb model with $\varepsilon = 0.111$, and correspond to the failure points labeled (a) and (b) on the corresponding failure surface shown in Fig. 12 (i.e., for load paths with $\tan\phi = 0.839$ and $\tan\phi = 0.700$, respectively). As expected from the corresponding critical displacement parameter surfaces, shown

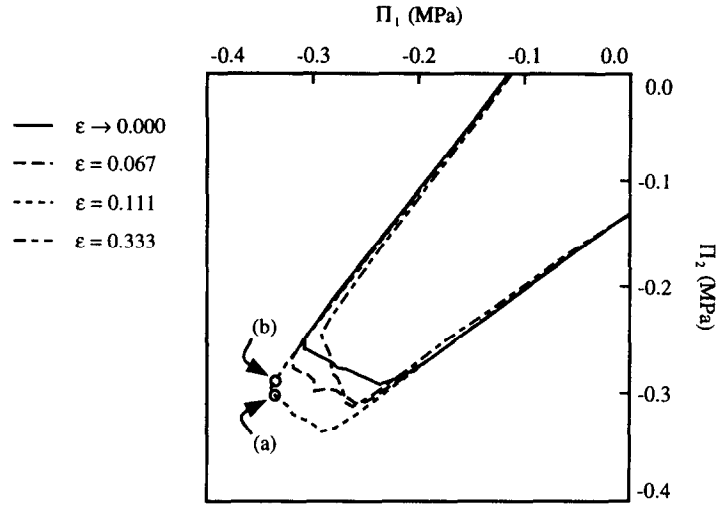

Fig. 12. Scale effects on the initial bifurcation surface for perfectly periodic honeycomb models, subjected to biaxial compression along the initial axes of material orthotropy ($\theta = 0$).

in Figs 2 and 3, respectively, the shape of the eigenmode for the local instability corresponding to point (a) is periodic (with a wavelength in each coordinate direction which is commensurate with the unit cell dimensions) near the center of the model (i.e., away from the boundaries), as shown in Fig. 13(a), while the shape of the eigenmode for the global instability, corresponding to point (b), varies smoothly over the entire specimen, as shown in Fig. 13(b).

3.6. *Sensitivity to imperfections*

Up to this point, it has been assumed that the undeformed honeycomb models ideally possess perfectly periodic microstructures, for which all unit cells are identical, all cell walls are straight, and the material properties are uniform. Aluminum honeycomb specimens used in engineering applications obviously contain imperfections due to variations in the initial material properties of the aluminum strips used in their fabrication, and also due to variations in the final microgeometry resulting from inaccuracies in the manufacturing process. Given that geometric and material property imperfections have similar effects on the failure surfaces of the honeycomb specimens, only imperfections in the microstructural geometry of the honeycomb models are presently considered.

Two categories of geometric imperfections are distinguished. The first category includes systematic imperfections, which are either due to variations in the bond lengths of the aluminum strips, or result from over- or under-expansion of the honeycomb specimen during the manufacturing process. These imperfections are equivalent, and result in nonregular hexagonal honeycombs, which, however, maintain their periodic microstructures (see Papka and Kyriakides, 1994). The second category of imperfections includes all random geometric imperfections, which can arise due to a variety of additional inaccuracies occurring during material fabrication.

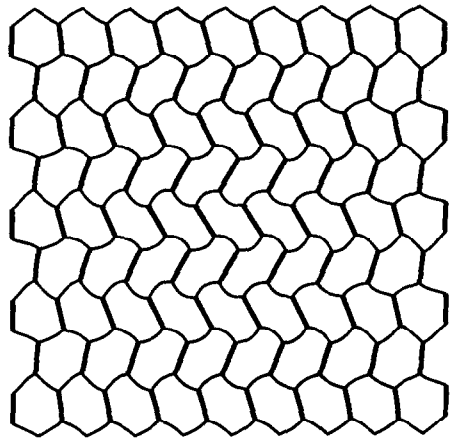

(a)

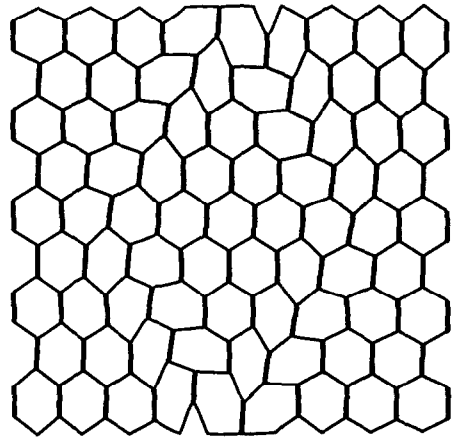

(b)

Fig. 13. Bifurcation mode shapes for finite honeycomb models with perfectly periodic microstructures exhibiting: (a) periodic wavelengths which are equal to the unit cell dimensions; and (b) wavelengths which are much larger than the unit cell dimensions.

Unlike the systematic imperfections, the random imperfections result in honeycombs with non-periodic microstructures.

Consider first the systematic imperfections, which are due to variations in the bond lengths along the honeycomb cell walls. Here, the imperfect honeycomb bond length is given by $\bar{l} = (1+\delta)l$, where δ is the bond length imperfection amplitude parameter, and l is the initially perfect material bond length (see the insert in Fig. 14(a)).

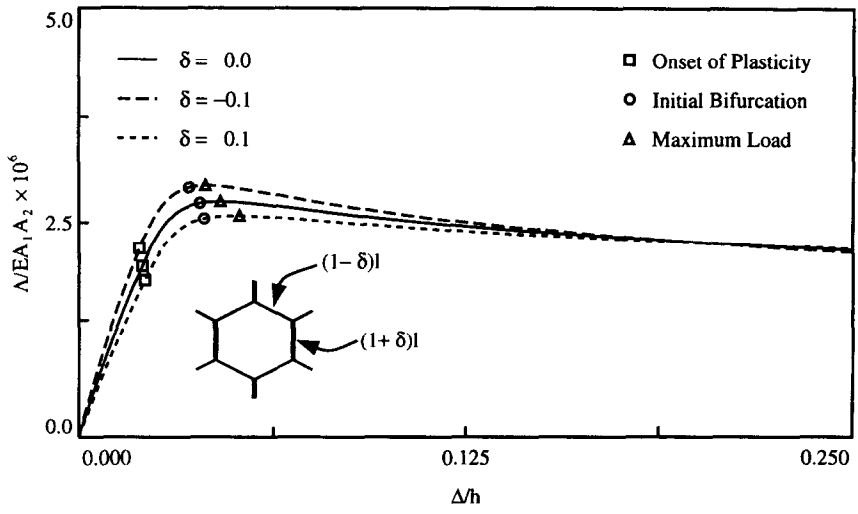

(a)

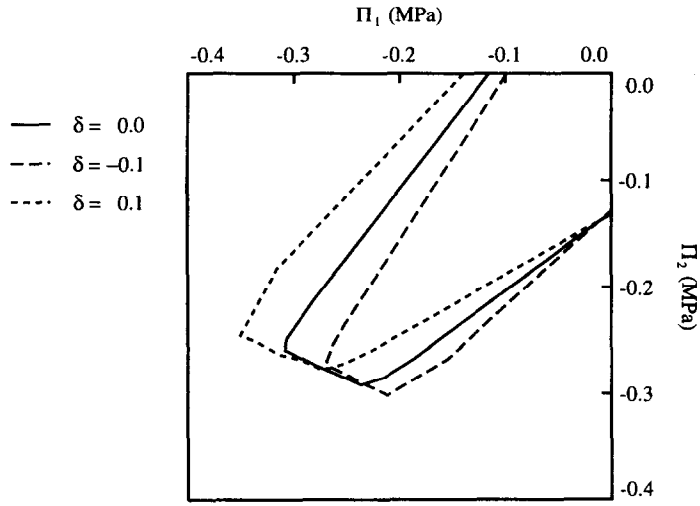

(b)

Fig. 14. Effects of systematic imperfections in the honeycomb material bond length on : (a) the dimensionless force–displacement response for an infinite honeycomb model, subjected to biaxial compression along the initial axes of material orthotropy ($\theta = 0$) with $\tan\phi = 2.747$; and (b) the corresponding initial bifurcation surfaces.

The effects of these imperfections on the behavior and the failure of the aluminum honeycombs are considered for models which are subjected to biaxial loadings along the initial axes of material orthotropy ($\theta = 0$). The influence of an imperfection in the material bond length, in the typical force-displacement response for the unit cell, is

shown in Fig. 14(a), for three different material bond lengths corresponding to values of the imperfection amplitude parameter ranging from $\delta = -0.1$ to $\delta = 0.1$. The results correspond to a load path with $\tan\phi = 2.747$, and indicate an increase in the load level for a decrease in the bond length, and conversely, a decrease in the load level for an increase in the bond length, for deformations occurring prior to $\Delta/h \approx 0.2$.

The influence of bond length imperfections on the initial bifurcation surface for an infinite honeycomb model is shown in Fig. 14(b). Notice that only a 10% change in bond length produces a significant effect on the initial bifurcation surface. This influence is due to significant changes in the unit cell behavior in the domain of plastic deformation. Note also, that in the elastic domain of deformation, where the failure surfaces coincide, the effects on the initial bifurcation surface are relatively insignificant.

The study of the effects of imperfections on the onset of failure is concluded with an investigation involving honeycomb models with random geometric imperfections. Unlike bond length imperfections, random geometric imperfections destroy the periodicity in the honeycomb microstructure. To model the geometry of the imperfect honeycombs, random perturbations in the initial (i.e., the undeformed) positions of the hexagon vertices are produced in a manner similar to that described for the idealized lattice models, presented in Schraad and Triantafyllidis (1997). The coordinates of a hexagon vertex in the perfectly periodic configuration are perturbed by $\Delta X_i = \delta c r_i$ $(i = 1, 2)$, where δ is the random geometric imperfection amplitude parameter, and r_i are random numbers satisfying the condition $-1 \leqslant r_i \leqslant 1$. In the ensuing calculations, two different values of the random geometric imperfection amplitude parameter are considered. The first, $\delta = 0.03$, corresponds to the Aluminum 5052-H39 honeycomb specimens used by Papka and Kyriakides (1994), and the second, $\delta = 0.10$, is an arbitrarily chosen upper bound.

Unlike the bond length imperfections, the random geometric imperfections result in behavior for which the initial bifurcation in the principal solution of the perfectly periodic specimen (depicted by the solid line) is replaced by a limit load in the force-displacement response of the finite specimen (depicted by the dashed and dotted lines), as shown in Fig. 15(a). Here, the response is calculated for a 9×9 hexagon cell specimen, subjected to biaxial compression along the initial axes of material orthotropy ($\theta = 0$) with $\tan\phi = 2.747$. For successive increases in the imperfection amplitude parameter, the maximum load in the imperfect honeycomb response experiences successive decreases. The maximum load surfaces for the imperfect, 9×9 hexagon cell specimens, with $\delta = 0.03$ and $\delta = 0.10$, are shown in Fig. 15(b), together with the initial bifurcation surface of the corresponding infinite, perfectly periodic model. As expected from the discussion of the results presented in Fig. 15(a), the failure surface determined for the infinite, perfectly periodic model provides an upper bound for the failure surfaces of the imperfect models. Note also, that for the honeycomb perturbed by the smaller random geometric imperfection amplitude parameter $\delta = 0.03$, the maximum load surface for the 9×9 hexagon cell specimen is relatively close to this upper bound.

It is of interest, at this point, to compare the theoretical results, obtained for the infinite, perfectly periodic honeycomb model, and the numerical results, obtained for the finite counterpart with microstructural imperfections, with similar results reported

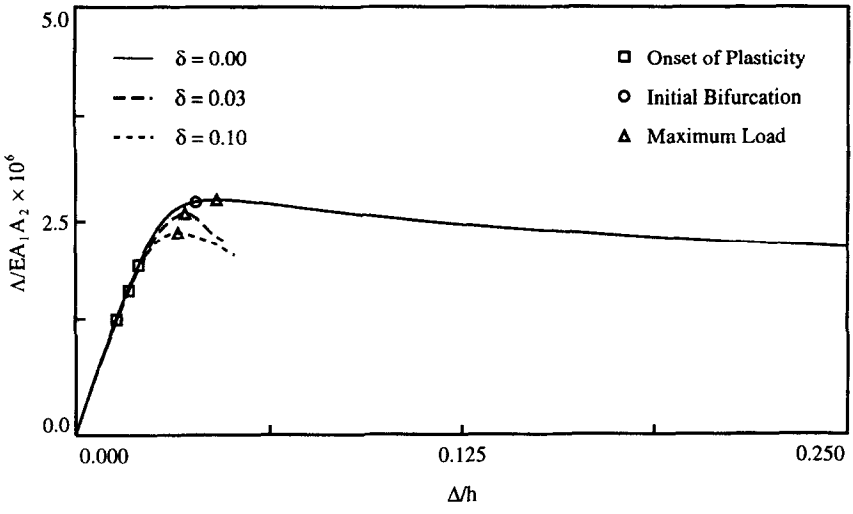

(a)

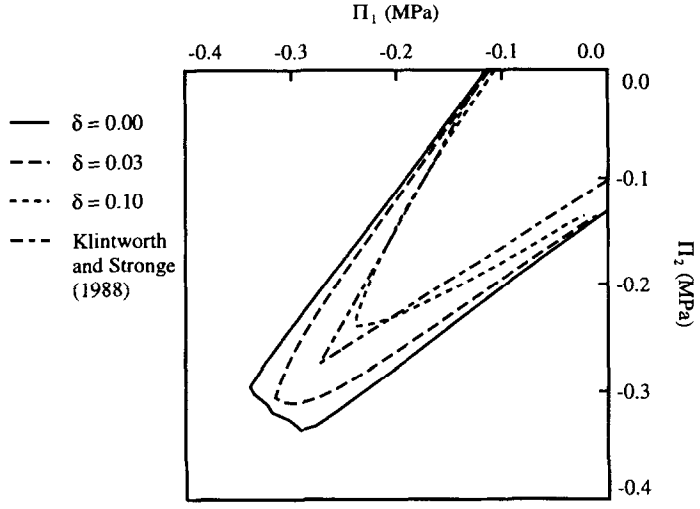

(b)

Fig. 15. Effects of random geometric imperfections in the honeycomb material microstructure on: (a) the dimensionless force–displacement response for an infinite honeycomb model, subjected to biaxial compression along the initial axes of material orthotropy ($\theta = 0$) with $\tan\phi = 2.747$; and (b) the corresponding failure surfaces for two different values of the imperfection amplitude parameter δ. The surface depicted by the dashed-dotted line represents the corresponding empirical failure surface estimate provided by Klintworth and Stronge (1988).

by other researchers. Preference for the work of Klintworth and Stronge (1988) on biaxially crushed honeycombs, for use in this comparison, is justified by the fact that their model is the most realistic (i.e., their model accounts for the doubled thickness

of the cell walls along the vertical direction of the honeycomb material). Their modeling effort consists of an elastic buckling analysis and a limit load calculation, both based soley on the unit cell of the model (differences in behavior between the infinite, perfectly periodic specimen and the finite specimens with microstructural imperfections are not considered in their work). An empirical approach, which combines the elastic buckling and limit load calculations, is used to determine two expressions (see eqns (6.2) and (6.3) on page 282 of Klintworth and Stronge, 1988), which provide reasonable upper bounds for the maximum loads encountered by their biaxially crushed honeycomb specimens (see also Fig. 11 on page 284). These same equations have been applied using the geometry and material properties of the honeycomb specimens considered in the present work, and the results (depicted by the dashed–dotted line) are plotted in Fig. 15(b). Note that the failure surface predictions of Klintworth and Stronge fall well inside the maximum load surfaces obtained for the honeycomb specimen with the realistic imperfection amplitude parameter $\delta = 0.03$, but intersect the corresponding failure surface obtained for the specimen with the larger amplitude of imperfection $\delta = 0.10$. Klintworth and Stronge give no quantitative measure of the geometric microstructural imperfections which may be present in the honeycomb specimens used in their experimental investigations. If the specimens used in their work are considerably larger in size than the 9×9 specimens considered in the present numerical investigation, then one can plausibly explain the fact that the maximum load surface obtained for the honeycomb specimen with $\delta = 0.03$ lies outside the estimate for the maximum load surface provided by Klintworth and Stronge.

The presence of a maximum load in the response of the imperfect specimen inevitably leads to localized deformation failure modes, as shown in Fig. 16. This deformed

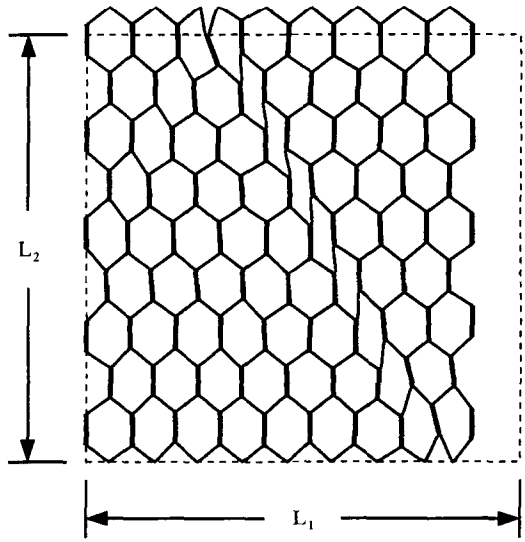

Fig. 16. Ultimate failure mechanism (i.e., localization of deformation) for a finite honeycomb model with random geometric imperfections in the material microstructure, subjected to biaxial compression along the initial axes of material orthotropy ($\theta = 0$) with $\tan\phi = 0.364$.

configuration was calculated for a finite honeycomb model, with $\delta = 0.03$, subjected to biaxial compression along the initial axes of material orthotropy ($\theta = 0$), with a principal stress ratio $\tan\phi = 0.364$. Note that the localized failure zone is oriented at an angle to the principal macroscopic stress axes. The determination of this angle involves an investigation of the postbuckling response of the infinite honeycomb model, which is a completely different (and more difficult) problem from the onset of instability problems addressed here. It should be emphasized at this point, that the postbuckling response, which reaches a rather extended load plateau as one row of cells collapses after another (see Papka and Kyriakides, 1994), determines the practical load carrying capacity of the honeycomb specimen. The reader interested in the postbuckling behavior of structures which exhibit a load maximum in their principal solution, is referred to the excellent review article of Kyriakides (1993).

4. CONCLUSIONS

Of interest in this work is the theoretical prediction of the onset of failure in aluminum honeycombs under arbitrary macroscopic loading conditions. Following a general theory for rate-independent, periodic solids, proposed by Triantafyllidis and Schnaidt (1993), a failure surface for the infinite, perfectly periodic medium is defined by the principal macroscopic stresses at the onset of the initial bifurcation instability encountered along proportional load paths. Therefore, the corresponding calculations are based on the equilibrium solutions for the unit cell along such load paths. Since cellular materials are often used in shock mitigation and energy absorption applications, the investigation is carried out for aluminum honeycombs subjected to in-plane, compressive stress states, and the resulting failure surfaces are presented in macroscopic stress space. In addition to the initial bifurcation surface for the perfectly periodic honeycomb of infinite extent, the failure surface corresponding to the onset of plastic deformation in each cell, and the failure surface corresponding to the maximum load, have also been determined and plotted in macroscopic stress space. All of the results reported here correspond to a commercially available aluminum honeycomb, for which the material properties have been determined experimentally by Papka and Kyriakides (1994).

Due to the high flexibility of the honeycomb unit cell under compressive stresses, the eigenmode corresponding to the first instability encountered during the proportional loading is either strictly periodic, with the same spatial periodicity as the hexagonal lattice model (in which case, the wave numbers of the bifurcation eigenmode along the X_1 and X_2 coordinate directions are $\omega_1 = \omega_2 = 0$), or is a long wavelength mode, with a period that is much larger than the unit cell dimensions (in which case, the corresponding wave numbers are $\omega_1 \to 0$ and $\omega_2 \to 0$). For the latter case, the onset of failure in the honeycomb specimen coincides with the loss of ellipticity of the homogenized moduli of the material (see Geymonat *et al.*, 1993), while in the former case, the homogenized incremental moduli cannot be defined. Hence, for the case of an aluminum honeycomb, the microscopic failure surface (for which the calculations are computationally time consuming) coincides with the macroscopic failure surface (which is much more easily obtained), introduced in Triantafyllidis and Schnaidt

(1993), thus explaining the omission of the macroscopic failure calculations in this work.

The results show that there is an extreme sensitivity of the onset of plasticity and maximum load surfaces, to the ratio of principal macroscopic stresses $\tan\phi$ and the macroscopic load orientation angle θ. It has been determined, for the case of biaxial loading along the initial axes of material orthotropy ($\theta = 0$), that a bifurcated solution always exists prior to reaching a maximum load, while a maximum load cannot be reached for macroscopic stress states approaching uniaxial compression. In addition, for load paths which include shear (e.g., for $\theta = \pi/4$), the situation is reversed; that is, a maximum load is always attained, but a bifurcated solution exists only for certain ratios of principal stresses. Moreover, depending on the principal stress ratio, a bifurcated solution can appear after the maximum load has been reached. In any event, the previously mentioned coincidence of the micro- and macro-failure surfaces, implies that localization of the postbuckling deformation will occur under all macroscopic loading conditions (see the discussion in Triantafyllidis and Bardenhagen, 1996).

The influence of the geometric scale parameter ε (i.e., the size of the unit cell, relative to the overall size of the honeycomb specimen) has also been studied, and the results show that the failure surfaces of the finite honeycomb specimens converge to the failure surface of their corresponding infinite counterpart as $\varepsilon \to 0$. The influence of imperfections in the honeycomb microstructure has been studied as well, for two different classes of imperfections: systematic imperfections, which simply change the geometry of the unit cell, while preserving the periodicity of the microstructure; and random geometric imperfections, which are inevitable in practice, and which destroy the periodicity of the microstructure. The practicality of determining the failure surface for the infinite, perfectly periodic honeycomb, lies in the fact that it is an upper bound for the failure surfaces of the specimens with random imperfections, as discussed in Schraad and Triantafyllidis (1997). Time consuming calculations for finite specimens with realistic, random geometric imperfections have been carried out, and the results have been compared with the failure predictions for the corresponding perfectly periodic specimens.

Unlike previous theoretical and experimental investigations, concerning the failure of periodic composites under plane strain conditions, the present study considers all possible macroscopic stress states (i.e., stress states for which the principal axes of stress are oriented at arbitrary angles to the initial axes of material orthotropy). The failure surface for the infinite, perfectly periodic specimen provides an upper bound for the stresses at the onset of failure in these materials (an upper bound which is relatively easy to calculate). Given that there exists a strong dependence of these failure surfaces on the macroscopic stress states, the proposed methodology offers a useful predictive tool for the design of aluminum honeycombs. Of course, the ultimate failure of these materials by localization of deformation occurs at lower loads. However, the theoretical prediction of these loads requires a much more sophisticated postbuckling analysis—a task which lies beyond the scope of this work.

Finally, it should be emphasized here that the methodology used in this work, to establish the failure surfaces for the aluminum honeycombs, is applicable to any rate-independent, periodic medium which undergoes finite deformations. This meth-

odology uses the construction of the micro-failure surface for the infinite, perfectly periodic specimen, which requires calculations based only on the unit cell, to provide an upper bound for the failure surfaces of the more realistic (i.e., the imperfect) microstructured media. This is advantageous, since the failure calculations involved in an actual application would be prohibitively time consuming. The ideas developed here have recently been applied to materials with continuum microstructures (see Triantafyllidis and Bardenhagen, 1996, for the case of fiber-reinforced composites), and these same ideas are currently being employed by the present authors in the study of some three-dimensional cellular solids.

ACKNOWLEDGEMENTS

The present work was partially funded, initially by Alcoa, and subsequently by AFOSR under Grant DOD-G-F49620-94-1-0402. The authors would like to express their appreciation for this financial assistance, and their gratitude to Dr Owen Richmond of the Alcoa Technical Center for his interest and encouragement, and for sharing his ideas on the subject of stability as it relates to microstructured materials. The authors are also indebted to Prof. S. Kyriakides of the University of Texas at Austin for his assistance, and for the many valuable discussions which arose during the course of this investigation.

REFERENCES

Antman, S. (1968) General solutions for plane extensible elasticae having nonlinear stress–strain laws. *Quart. Appl. Math.* **26,** 35–47.

Ashby, M. F. (1983) The mechanical properties of cellular solids. *Metall. Trans.* **14A,** 1755–1769.

Gent, A. N. and Thomas, A. G. (1963) Mechanics of foamed elastic materials. *Rubb. Chem. Technol.* **36,** 597–610.

Geymonat, G., Müller, S. and Triantafyllidis, N. (1993) Homogenization of nonlinearly elastic materials, microscopic bifurcation and macroscopic loss of rank-one convexity. *Arch. Rat. Mech. Anal.* **122,** 231–290.

Gibson, L. J. and Ashby, M. F. (1982) The mechanics of three-dimensional cellular materials. *Proceedings of the Royal Society of London* **A382,** 43–59.

Gibson, L. J. and Ashby, M. F. (1988) *Cellular Solids: Structure and Properties.* Pergamon Press, Oxford.

Gibson, L. J., Ashby, M. F., Schajer, G. S. and Robertson, C. I. (1982) The mechanics of two-dimensional cellular materials. *Proceedings of the Royal Society of London* **A382,** 25–42.

Gibson, L. J., Ashby, M. F., Zhang, J. and Triantafillou, T. C. (1989) Failure surfaces for cellular materials under multiaxial loads—I. Modeling. *Int. J. Mech. Sci.* **31,** 635–663.

Hilyard, N. C., ed. (1982) *Mechanics of Cellular Plastics.* Macmillan, New York.

Klintworth, J. W. and Stronge, W. J. (1988) Elasto-plastic yield limits and deformation laws for transversely crushed honeycombs. *Int. J. Mech. Sci.* **30,** 359–378.

Klintworth, J. W. and Stronge, W. J. (1989) Plane punch indentation of a ductile honeycomb. *Int. J. Mech. Sci.* **31,** 273–292.

Kyriakides, S. (1993) Propagating instabilities in structures. In *Advances in Applied Mechanics,* ed. W. Hutchinson and T. Y. Wu, Vol. 30. Academic Press, Boston.

Love, A. E. H. (1944) *A Treatise on the Mathematical Theory of Elasticity.* Dover, New York.

Papka, S. D. and Kyriakides, S. (1994) In-plane compressive response and crushing of honeycomb. *J. Mech. Phys. Solids* **42,** 1499–1532.

Patel, M. R. and Finnie, I. (1970) Structural features and mechanical properties of rigid cellular plastics. *J. Mater.* **5,** 909–932.

Schraad, M. and Triantafyllidis, N. (1997) Scale effects in media with periodic and nearly periodic microstructures—Part II: Failure mechanisms. *Journal of Applied Mechanics* **64,** 763–771.

Shaw, M. C. and Sata, T. (1966) The plastic behavior of cellular materials. *Int. J. Mech. Sci.* **8,** 469–478.

Triantafillou, Zhang, J., Shercliff, Gibson, L. J. and Ashby, M. F. (1989) Failure surfaces for cellular materials under multiaxial loads—II. Comparison of models with experiment. *Int. J. Mech. Sci.* **31,** 665–678.

Triantafyllidis, N. and Bardenhagen, S. (1996) The influence of scale size on the stability of periodic solids and the role of associated higher order gradient continuum models. *Journal of the Mechanics and Physics of Solids* **44,** 1891–1928.

Triantafyllidis, N. and Maker, B. N. (1985) On the comparison between microscopic and macroscopic instability mechanisms in a class of fiber-reinforced composites. *Journal of Applied Mechanics* **52,** 794–800.

Triantafyllidis, N. and Samanta, S. K. (1986) Bending effects on flow localization in metallic sheets. *Proceedings of the Royal Society of London* **A406,** 205–226.

Triantafyllidis, N. and Schnaidt, W. C. (1993) Comparison of microscopic and macroscopic instabilities in a class of two-dimensional periodic composites. *Journal of the Mechanics and Physics of Solids* **41,** 1533–1565.